H2 Mobility And Redox Control In Open Vs. Closed Hydrothermal Oceanic Systems – Evidence From Serpentinization Experiments

Colin Fauguerolles, Teddy Castelain, Johan Villeneuve, Michel Pichavant

Eur. J. Mineral., 36, 555–579, 2024
https://doi.org/10.5194/ejm-36-555-2024

European Journal of Mineralogy
Open Access

H_2 mobility and redox control in open vs. closed hydrothermal oceanic systems – evidence from serpentinization experiments

Colin Fauguerolles[1,2], Teddy Castelain[1], Johan Villeneuve[1,3], and Michel Pichavant[1]

[1]Institut des Sciences et de la Terre d'Orléans, UMR 7327, Orléans, France
[2]Laboratoire de Planétologie et de Géosciences, UMR 6112, Nantes, France
[3]Centre de Recherches Pétrographiques et Géochimiques, UMR 7358, Vandœuvre-lès-Nancy, France

Correspondence: Colin Fauguerolles (colin.faug@protonmail.com)

Received: 11 August 2023 – Revised: 9 April 2024 – Accepted: 10 April 2024 – Published: 3 July 2024

Abstract. New hydrothermal experiments in rapid-quench pressure vessels have been performed to investigate the effect of redox state on the serpentinization reaction. The experimental hydrogen fugacity (f_{H_2}) was controlled by monitoring the mobility of H_2 in the reacting system (internal vs. external f_{H_2} control). This was achieved by using either Au (H_2 impermeable) or AgPd (H_2 permeable) capsules and Ar pressurizing gas to control f_{H_2}. The experiments were performed with either San Carlos olivine powders or Åheim dunite chips. Water / rock mass ratios of 1–2, a total pressure of 50 MPa, and temperatures of 300 and 350 °C were investigated. Experimental durations of 30, 45, or ≈ 80 d were imposed. Serpentine production is observed in almost all experiments but is favored at 300 °C under external f_{H_2} control. The serpentine–magnetite assemblage is observed in Au capsules (high f_{H_2}) at 300 °C, while the serpentine–hematite(–magnetite) is observed in AgPd capsules (low f_{H_2}). At 350 °C, less H_2 is produced than at 300 °C and the serpentine–hematite(–magnetite) assemblage is present in both Au and AgPd capsules. Brucite is absent and this is interpreted to reflect both the initially oxidizing conditions and relatively low serpentine production in our experiments. Differences in product phase assemblages found in this study imply that natural serpentinization reaction mechanisms vary with redox conditions, and consequences for H_2 production fluxes and rates can be expected. The high-f_{H_2} (reduced) internally controlled experiments simulate low-permeability "closed" oceanic hydrothermal systems. The low-f_{H_2} (oxidized) externally controlled experiments are analogous to "open" oceanic hydrothermal systems where serpentinization is driven by tectonically aided infiltration of an external fluid.

1 Introduction

At slow-spreading ridges, tectonic expansion coupled with low magma production allows the outcropping of large volumes of mantle rocks on the ocean floor (Karson et al., 1987; Cannat, 1993). Interaction between seawater and peridotite leads to important modifications of the physical (i.e., rheology, magnetic signature, porosity, density, and permeability; Toft et al., 1990; Escartín et al., 1997, 2001; Oufi et al., 2002; Iyer et al., 2008; Plümper et al., 2012; Kelemen and Hirth, 2012; Rouméjon and Cannat, 2014; Maffione et al., 2014; Evans et al., 2020; Malvoisin et al., 2020) and chemical (i.e., mineral phase assemblages, compositions of solid and fluid phases; Mével, 2003; Bach et al., 2006; Andreani et al., 2007; Evans, 2008; Cannat et al., 2010; Charlou et al., 2010; Seyfried et al., 2011, 2015; Frost et al., 2013; Klein et al., 2014, 2019; Huang et al., 2017a) properties of mantle rocks at crustal scale – a process named serpentinization.

One of the most distinctive features of serpentinization environments is the generation of large amount of H_2 caused by the oxidation of ferrous iron (Fe^{2+}), contained in peridotitic minerals, coupled with the reduction of water (Neal and Stanger, 1983; Abrajano et al., 1990; Charlou et al., 2002). The produced ferric iron (Fe^{3+}) is incorporated into precipitating phases such as serpentine, wherein Fe is either partly or mostly Fe^{3+} (Klein et al., 2009; Marcaillou et al., 2011;

Andreani et al., 2013), as well as in magnetite ($Fe^{2+}Fe_2^{3+}O_4$), a common phase of serpentinites (Toft et al., 1990; Oufi et al., 2002; Klein et al., 2014; Maffione et al., 2014). In comparison, hematite ($\alpha Fe_2^{3+}O_3$) has been infrequently observed in CO_2-free experimental serpentinizing systems (Godard et al., 2013), although its formation as a reaction product of serpentinization has been theoretically considered (Frost, 1985; Evans et al., 2013; Malvoisin, 2015; Ely et al., 2023). The rare natural occurrences of hematite-bearing serpentinites have been attributed to the transformation of magnetite by fluid / rock interactions subsequent to serpentinization (Bach et al., 2004). Awaruite (Fe_3^0Ni), another Fe-bearing phase commonly present in serpentinites (Chamberlain et al., 1965; Frost, 1985; Klein and Bach, 2009), implies a reduction of Fe^{2+}. This diversity of solid phases involving Fe^0, Fe^{2+}, and Fe^{3+} highlights the potential of serpentinization process to involve apparently opposed and complex changes in redox state. Yet, apart from a few studies (Frost, 1985; Evans et al., 2013; Frost et al., 2013; Lazar, 2020), changes in redox state in serpentinites have remained largely descriptive (based on mineral Fe^{2+}/Fe^{3+} ratios) and not interpreted in a quantitative framework involving the redox variables: f_{O_2} (oxygen fugacity) and f_{H_2} (hydrogen fugacity).

The chemical aspects of serpentinization, i.e., fluid–rock reactions, have been investigated theoretically (Frost, 1985; Evans, 2008; Evans et al., 2013). They have led to numerous experimental (e.g., Martin and Fyfe, 1970; Moody, 1976; Seyfried and Dibble, 1980; Wegner and Ernst, 1983; Janecky and Seyfried, 1986; Berndt et al., 1996; McCollom and Seewald, 2001; Allen and Seyfried, 2003; Seyfried et al., 2007; Marcaillou et al., 2011; Hövelmann et al., 2011; Okamoto et al., 2011; Lafay et al., 2012, 2018; Malvoisin et al., 2012b, a; Mayhew et al., 2013; Klein and McCollom, 2013; Ogasawara et al., 2013; Malvoisin and Brunet, 2014; Klein et al., 2015; McCollom et al., 2016, 2020a, b; Syverson et al., 2017; Lamadrid et al., 2017, 2021; Huang et al., 2017a, b, 2019; Tutolo et al., 2018; Oyanagi et al., 2020; Klein and Le Roux, 2020) and thermodynamic studies, the latter based on reaction path models (Sleep et al., 2004; McCollom and Bach, 2009; Klein et al., 2009, 2013; Malvoisin, 2015; Ely et al., 2023). The importance of reaction kinetics has been recently demonstrated (Seyfried et al., 2007; Malvoisin et al., 2012a; Godard et al., 2013; Lamadrid et al., 2017, 2021; Tutolo et al., 2018; Oyanagi et al., 2020), and the evolution of the Fe speciation has been monitored during fluid circulation and fluid–rock interaction (Marcaillou et al., 2011; Andreani et al., 2013; Syverson et al., 2017). However, serpentinization is a reactive transport process which combines rock deformation, fluid circulation, and fluid–rock reaction (Steefel et al., 2005; Andreani et al., 2007; Godard et al., 2013; Klein et al., 2015). Natural serpentinizing systems are open to external fluids inputs. Temperature, water / rock ratios (W/R), and redox variables can vary with time and space, leading to variable extents of serpentinization and H_2 fluxes (Andreani et al., 2013). Thus, there is an increasing need to couple the chemical and the physical aspects of serpentinization, in particular the hydrodynamic regime of fluid circulations.

The impact of the fluid / rock ratio on serpentinization has been explored in several thermodynamic studies (Klein et al., 2013; Malvoisin, 2015; Ely et al., 2023). Comparatively few efforts have been put into experimentally coupling fluid–rock reaction and fluid circulation (Godard et al., 2013; Farough et al., 2016; Tutolo et al., 2018; Peuble et al., 2019; Osselin et al., 2022). In this paper, we present a set of hydrothermal experiments that enable the effect of H_2 mobility on the serpentinization reaction to be discussed. Conceptually, the mobility of H_2 is used as a proxy of fluid circulation, open vs. closed, in oceanic hydrothermal systems. H_2 is the closest to a perfectly mobile component (i.e., components whose chemical potential in the system is imposed by an external reservoir; Weill and Fyfe, 1964; Korzhinskii, 1965), and f_{H_2} is the key redox variable in hydrous systems (e.g., Eugster, 1957; Scaillet et al., 1992). In this paper, experiments have been designed in an original way enabling the mobility of H_2 to be controlled and varied. Below, the experimental and analytical methodologies are presented and the experimental result detailed. We show that significant differences appear in experimental phase assemblages and proportions, and in extents of reaction depending on H_2 mobility, and discuss the implication for serpentinization processes at mid-ocean ridges (MORs).

2 Background

In the following, redox states will be expressed preferentially in terms of f_{H_2} and to a lesser extent in terms of f_{O_2}. The f_{H_2} is a directly measurable variable (Shaw, 1963), and redox states can be conveniently varied experimentally by changing the f_{H_2} (Chou, 1987; Chou and Cygan, 1990; Scaillet et al., 1992; Schmidt et al., 1995). In hydrous systems, the two redox variables, f_{H_2} and f_{O_2}, are related through the following equilibrium:

$$H_2(g) + \frac{1}{2}O_2(g) \rightleftharpoons H_2O(g), \tag{R1}$$

whose equilibrium constant ($K_{(R1)}$) is

$$K_{(R1)} = \frac{f_{H_2O}}{f_{H_2} \times f_{O_2}^{1/2}}, \tag{1}$$

where f_{H_2O} is the fugacity of water. From Eq. (1), f_{H_2} can be expressed as

$$\log f_{H_2} = \log f_{H_2O} - \frac{1}{2}\log f_{O_2} - \log K_{(R1)}, \tag{2}$$

which illustrates that, for a hydrothermal fluid at constant T, f_{H_2O}, and total pressure (P_{Tot}), f_{H_2} varies linearly opposite to f_{O_2}. The mole fractions of the fluid components (H_2, O_2,

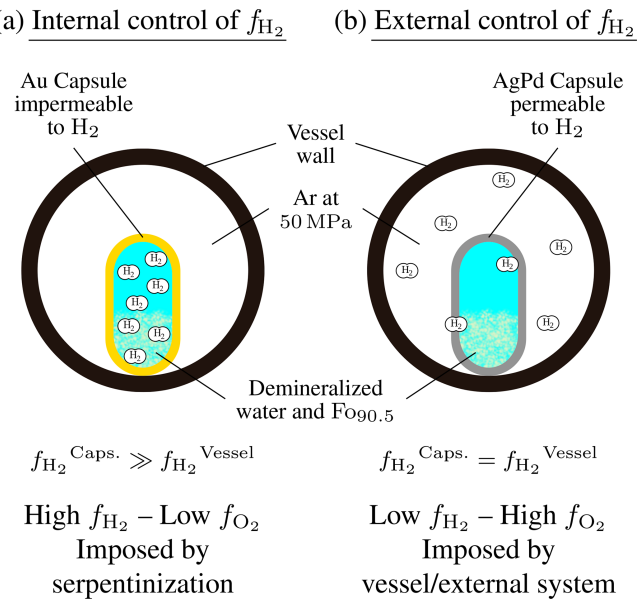

Figure 1. Illustration of the two types of experimental f_{H_2} control developed in this study. **(a)** Internal control of f_{H_2}. The serpentinization reaction takes place inside an Au capsule impermeable to H_2. This allows accumulation of H_2 inside the capsule along with advancement of the reaction and leads to high f_{H_2} and low f_{O_2}. **(b)** External control of f_{H_2}. The serpentinization reaction is performed in an AgPd capsule permeable to H_2. The external fluid (Ar pressurizing gas) imposes a constantly low f_{H_2} to the system. H_2 generated inside the capsule by the reaction is continuously extracted. This leads to low f_{H_2} and high f_{O_2}.

and H_2O) are related to their respective fugacities by the following general relation:

$$f_i = \phi_i \times X_i \times P_{Tot}, \quad (3)$$

where ϕ_i is the fugacity coefficient of component i and X_i the mole fraction of i in the fluid mixture. For most common geological fluids, X_{O_2} is negligible, whereas X_{H_2} is readily measurable, reaching values in the same range as X_{H_2O} under very reducing conditions (Eugster and Skippen, 1967; Frost et al., 2013). For example, at 300 °C and 50 MPa, $f_{H_2} = 2.1 \times 10^{-4}$ MPa for an oxidizing f_{O_2} corresponding to the hematite–magnetite (HM) buffer, while, for a reducing f_{O_2} corresponding to the fayalite–magnetite–quartz (FMQ) buffer, $f_{H_2} = 1.7 \times 10^{-1}$ MPa (Table 1).

Below, two cases will be considered depending on how the f_{H_2} variable is controlled. In the first case, the f_{H_2} variable is controlled internally; i.e., H_2 is produced by the advancement of the serpentinization reaction and allowed to accumulate in the reacting system (internal f_{H_2} control; Fig. 1a). In the second case, f_{H_2} is imposed externally from outside the reacting system (external f_{H_2} control; Fig. 1b).

3 Materials and methods

3.1 Starting materials

Two distinct starting materials were used in the experiments: San Carlos olivine and Åheim dunite. The San Carlos olivines ($Fo_{90.5}$; see Table A1 in Appendix A for detailed composition) were separated by hand from slightly disaggregated San Carlos xenoliths. In order to eliminate all contaminants (spinels, pyroxenes), only grains with a sufficient size (larger than ≈ 500 µm to allow a precise examination with binoculars) were kept. After several ultrasonic cleanings followed by abundant rinsing with deionized water, all crystals suspected of surface or inclusion contamination were removed. The Åheim dunite contains, in addition to olivine ($Fo_{94.0}$; Table A1), about 10 vol % orthopyroxene ($En_{93.9}$; Table A1), 0.5 vol %–1 vol % chromite, and 1 vol %–5 vol % clinochlore. Hydrous silicates such as serpentine, talc, phlogopite, and tremolite have been reported to be present in trace amounts (Berckhemer et al., 1982; Jackson et al., 1992), although none were found from SEM examination. In the same way and in contrast with the observations of (Jackson et al., 1992), no magnetite was observed in our Åheim dunite sample. This is consistent with the magnetic data (low magnetite mass fraction (MMF) of 2.5×10^{-3} wt %; see Sect. 3.4).

3.2 Experimental charges and capsules

Experimental parameters are summarized in Table 2. The San Carlos olivines were used in powder form, obtained by grinding the olivine crystals in an agate mortar. The resulting powders were sieved to different granulometric fractions: 0.5–1 mm, 45–50 µm, 25–32 µm, and < 10 µm. Above 32 µm, granulometric separations were performed with stainless-steel sieves. Below 32 µm, granulometric separations were performed with nylon sieves and a vibrating table. In both cases, powders were abundantly rinsed with deionized water in order to remove the smallest particle sizes. The Åheim dunite was used as experimental starting materials in the form of millimeter-sized chips. Experimental charges, consisting of either the olivine or the dunite (R) plus demineralized water (W), were loaded in noble metal capsules (4.2 or 5 mm diameter, 30–35 mm length, wall thickness 0.2 mm) which were welded shut. Capsules were weighted at each step during preparation and cooled during welding to ensure that no water loss occurred. Masses of reactants were adjusted to yield W/R ratios of either 1 or 2 (Table 2). Capsules were checked for leaks (by placing them in an oven and weighting) and then inserted in the pressure vessel.

Control of f_{H_2} was achieved by using two different capsule materials, Au and $Ag_{25}Pd_{75}$ or $Ag_{23}Pd_{77}$ (wt %; AgPd in the following text). Au capsules are almost impermeable to H_2 at the temperatures investigated in this study (Gunter et al., 1987). Therefore, in experiments performed with Au capsules, the f_{H_2} is intrinsically controlled by and depends

Table 1. Calculated f_{H_2} and f_{O_2} for HM and FMQ buffers at 300 and 350 °C and 50 MPa.

Buffer	T (°C)	ϕ_{H_2} [a]	ϕ_{H_2O} [b]	log $K_{(R1)}$ [c]	f_{H_2O} (MPa)	f_{H_2} (MPa)	log(f_{O_2}) (MPa)
FMQ[d]	300	1.187	0.167	19.633	8.33	1.66×10^{-1}	−36.87
HM[e]	300	1.187	0.167	19.633	8.35	2.10×10^{-4}	−31.08
FMQ	350	1.17	0.277	17.843	13.80	2.12×10^{-1}	−33.06
HM	350	1.17	0.277	17.843	13.85	3.50×10^{-4}	−27.49

Calculations are made using a Lewis and Randall mixing rule for the H_2O–H_2 fluid. [a] From Shaw and Wones (1964). [b] From Burnham et al. (1969). [c] Calculated with SUPCRT92 from Johnson et al. (1992). [d] From Myers and Eugster (1983) in Chou (1987). [e] From Haas and Robie (1973) in Chou (1987).

Table 2. Experimental parameters and summary of results obtained on solid products.

Experiment	Capsule material	Grain size (µm)	T (°C)	Duration (h)	Mass of water (mg)	Mass of solid (mg)	W/R ratio	Phase assemblage XRD	Phase assemblage SEM	Fe–Ox Raman	MMF[a] (wt %)	S[b] (%)
San Carlos olivine												
ol300AuG	Au	500–1000	300	2010	100.8	50.5	2.00	Ol	Ol–Ct–FeOx	Mgt	0.056	0.9
ol300PdG	$Ag_{25}Pd_{75}$[c]	500–1000	300	2010	96.9	50.0	1.94	Ol	Ol–Ct–FeOx	Hm–Mgt	0.003	
ol300Au45	Au	45–50	300	720	145.4	73.4	1.98	Ol	Ol–Ct–FeOx	nd[d]	0.080	1.3
ol300Pd45	$Ag_{25}Pd_{75}$	45–50	300	722	148.4	75.0	1.98	Ol–Srp–Hm	Ol–Ct–FeOx	nd	0.007	
ol300Au10	Au	< 10	300	720	140.8	77.2	1.82	Ol–Srp–Mgt	na[e]	nd	0.340	5.4
ol300Pd10	$Ag_{25}Pd_{75}$	< 10	300	720	149.3	74.3	2.01	Ol–Srp–Hm	na	nd	0.057	
ol350AuG	Au	500–1000	350	1782	98.5	49.9	1.97	Ol	Ol–Ct–FeOx	Hm–Mgt	0.002	
ol350PdG	$Ag_{25}Pd_{75}$	500–1000	350	1800	98.8	50.1	1.97	Ol	Ol–Ct–FeOx	Hm–Mgt	0.001	
ol350Au45	Au	45–50	350	738	149.9	74.7	2.01	Ol	Ol–Ct–FeOx	nd	0.017	
ol350Pd45	$Ag_{25}Pd_{75}$	45–50	350	719	149.5	75.8	1.97	Ol	Ol–Ct–FeOx	nd	0.009	
ol350Au25	Au	25–32	350	738	150.4	74.7	2.01	Ol	Ol–Ct–FeOx	nd	0.012	
ol350Pd25	$Ag_{25}Pd_{75}$	25–32	350	719	148.7	74.8	1.99	Ol	Ol–Ct–FeOx	nd	0.020	
ol350Au10	Au	< 10	350	716	155.9	80.7	1.93	Ol–Srp	na	nd	0.020	
ol350Pd10	$Ag_{23}Pd_{77}$[c]	< 10	350	709	138.1	70.0	1.97	Ol–Srp–Mgt–Hm	na	nd	0.938	
Åheim dunite												
du350AuG	Au	≈ 2000	350	1058	97.9	100.2	0.98	Ol–Opx–Chl	Ol–Opx–Chl–Chr	nd	0.010	
du350PdG	$Ag_{23}Pd_{77}$	≈ 2000	350	1045	150.3	150.1	1.00	Ol–Opx–Chl	Ol–Opx–Chl–Ct	nd	0.030	
								Mgh	Chr–FeOx–FeNiS		(0.036)[f]	

[a] MMF: magnetite mass fraction, calculated as explained in text. [b] S: reaction progress, calculated with model proposed by Malvoisin et al. (2012b); see text. [c] $Ag_{23}Pd_{77}$ and $Ag_{25}Pd_{75}$ capsules are indifferently used (the differences of composition are too small to lead a perceptible effect in terms of H_2 permeability). [d] nd: not determined. In spite of numerous attempts the type of iron oxides of these samples could not be determined; see text. [e] na: not analyzed. [f] Value in brackets corresponds to the mass fraction of maghemite (considering the maghemite as the only one responsible for the increase of J_s; see text). Mineral abbreviations: Ol: olivine; Opx: orthopyroxene; Chl: clinochlore; Srp: serpentine; Ct: chrysotile; FeOx: unspecified Fe oxide; Mgt: magnetite; Hm: hematite; Mgh: maghemite; Chr: chromite; FeNiS: Fe–Ni sulfide.

on the advancement of the serpentinization reaction (internal f_{H_2} control). H_2 accumulates inside the capsule, and this leads to high-f_{H_2} and thus low-f_{O_2} conditions (Fig. 1a). Our experimental setup does not allow a direct measurement of f_{H_2} inside Au capsules. However, the f_{H_2} can be estimated from the H_2 molality in hydrothermal fluids (m_{H_2}) determined in other closed-system olivine serpentinization experiments (Berndt et al., 1996; Allen and Seyfried, 2003; McCollom et al., 2016; Fauguerolles, 2016). The f_{H_2} and the m_{H_2} are related by

$$f_{H_2} = \gamma_{H_2} \times m_{H_2} \times K_{(R2)}, \quad (4)$$

where $K_{(R2)}$, computed in the following using SUPCRT92 (Johnson et al., 1992), is the equilibrium constant of

$$H_2(aq) \rightleftharpoons H_2(g), \quad (R2)$$

and γ_{H_2} is the molar activity coefficient of H_2(aq). The latter can be assimilated to the molar activity coefficient of CO_2(aq) (Garrels and Thompson, 1962), itself calculated from the work of Drummond (1981). Experimental m_{H_2} data used to constrain f_{H_2} in our closed-system experiments are detailed in Table 3. When interpolated at 720 h, the typical duration of our experiments, f_{H_2} at 300 °C varies between 4.78 and 0.18 MPa, which corresponds to $\Delta HM = -8.77$ and $\Delta HM = -5.89$, respectively. Differences in f_{H_2} between studies reflects the difference in grain size, smaller in the experiments of Berndt et al. (1996) and Fauguerolles (2016), which increases the reaction rate and associated H_2 production and increases f_{H_2}. Reaction path models (Klein et al., 2013) predict a maximum production of H_2 around 322 °C followed by a drastic decrease at higher temperatures.

Table 3. f_{H_2} and corresponding f_{O_2} and ΔHM calculated using previously published m_{H_2} associated with $Fo_{88–91}$ serpentinization.

Study	T (°C)	P_{Tot} (MPa)	log $K_{(R2)}$[a]	Grain size (µm)	W/R ratio	Duration (h)	m_{H_2} (mmol kg^{-1})	f_{H_2} (MPa)	log(f_{O_2}) (MPa)	ΔFMQ (log unit)	ΔHM (log unit)
Experimental measurements											
Berndt et al. (1996)	300	500	2.535	< 75	2.25	674	108	4.67	−39.83	−2.96	−8.75
						720[b]	**110**	**4.78**	**−39.85**	**−2.98**	**−8.77**
						1658	158	6.84	−40.20	−3.33	−9.12
McCollom et al. (2016)	300	350	2.485	53–212	2.1	11	0.45	0.017	−34.96	1.93	−3.88
						720	**4.6**	**0.18**	**−36.98**	**−0.08**	**−5.89**
						1172	7.2	0.28	−37.37	−0.48	−6.29
	320	350	2.383	53–212	2.5	481	0.75	0.023	−33.53	1.77	−3.95
						720	**1.0**	**0.032**	**−33.81**	**1.48**	**−4.23**
						1343	1.8	0.056	−34.29	1	−4.71
Fauguerolles (2016)	300	500	2.535	< 60	1.62	713.5	85	3.77	−39.63	−2.76	−8.55
						720	**85**	**3.78**	**−39.63**	**−2.77**	**−8.56**
						1056	100	4.43	−39.78	−2.91	−8.70
	350	500	2.279	< 60	1.82	509	8	0.21	−33.03	0.03	−5.54
						720	**9**	**0.23**	**−33.12**	**−0.06**	**−5.63**
						983	13	0.33	−33.46	−0.4	−5.96
Allen and Seyfried (2003)	400	500	1.956	≈ 60	4	672	2.3	0.033	−28.04	1.77	−3.60
						720	**2.2**	**0.032**	**−28.02**	**1.80**	**−3.58**
						1032	1.8	0.026	−27.83	1.98	−3.39
Reaction path calculations											
Klein et al. (2013)	250	500	2.764				191	13.5	−45.72	−4.32	−10.37
	300	500	2.535				295	12.8	−40.85	−3.98	−9.77
	350	500	2.279				18	0.45	−33.72	−0.66	−6.22
This study											
Au capsules	300	500	2.535	1000 to < 10	2	720–2000		0.18 to 4.78[c]	−36.98 to −39.85	−0.08 to −2.98	−5.89 to −8.77
AgPd capsules	300	500	2.535	1000 to < 10	2	720–2000		2.1×10^{-4}	−31.08	5.79	0
Au capsules	350	500	2.279	1000 to < 10	2	720–2000		0.032 to 0.23	−31.41 to −33.12	1.64 to −0.06	−3.92 to −5.63
AgPd capsules	350	500	2.279	1000 to < 10	2	720–2000		0.9×10^{-4}	−26.31	6.75	1.19

[a] Calculated with SUPCRT92 from Johnson et al. (1992). [b] Values in bold are calculated by linear interpolation of m_{H_2} at 720 h, the duration of the majority of our experiments. [c] See text for details about the f_{H_2} range in Au capsules.

This significant drop in f_{H_2} is observed between 300 and 320 °C by McCollom et al. (2016), from $f_{H_2} = 0.18$ MPa ($\Delta HM = -5.89$) at 300 °C to $f_{H_2} = 0.032$ MPa ($\Delta HM = -4.23$) at 320 °C, and by Fauguerolles (2016) between 300 and 350 °C, from $f_{H_2} = 3.78$ to 0.23 MPa ($\Delta HM = -8.56$ to -5.63). We also note that the 400 °C experiment of Allen and Seyfried (2003) yields the same f_{H_2} (0.032 MPa) as that of McCollom et al. (2016) at 320 °C. Based on these results, the f_{H_2} in our closed-system experiments can be estimated to be bracketed between 0.18 and 4.78 MPa at 300 °C and between 0.032 and 0.23 MPa at 350 °C.

In contrast, AgPd capsules are quite permeable to H_2. At 300 °C, H_2 permeability is 9 log units higher in AgPd than in Au and 8 log units higher at 350 °C (Gunter et al., 1987). By using a H_2 permeable capsule, the f_{H_2} inside the capsule becomes rapidly equal to the f_{H_2} outside the capsule (i.e., of the pressurizing gas). Volume considerations (the volume of pressurized gas in the vessel is about 10 cm^3, whereas the volume of the experimental capsule is about 0.1 cm^3) dictate that, in this case, the f_{H_2} within the capsule is imposed by the f_{H_2} of the pressurizing gas (external f_{H_2} control; Fig. 1b). The f_{H_2} imposed by the Ar pressurizing gas has been constrained both directly and indirectly (see Appendix B). At 350 °C, 50 MPa, the f_{H_2} is 0.9×10^{-4} MPa, which corresponds to $\Delta HM = +1.19$. At 300 °C, no such measurements are available, but the temperature dependence of the f_{H_2} in such an oxidizing f_{O_2} range is small, and a maximum f_{H_2} of 2.1×10^{-4} MPa (corresponding to the value of the HM buffer at 300 °C; Table 1) can be assumed. Therefore, our internally and externally controlled experiments differ by 3.45–4.4 log units in f_{H_2} (5.9–8.8 log units in f_{O_2}) at 300 °C and, at 350 °C, by 2.55–3.4 log units in f_{H_2} (5.1–6.8 log units in f_{O_2}).

Below, experiments will be designated by type of starting material (*ol* for San Carlos olivine, *du* for Åheim dunite), temperature (*300* for 300 °C, *350* for 350 °C), capsule material (*Au* for Au, *Pd* for AgPd), and initial grain size (*G* for 0.5–1 mm, *45* for 45–50 µm, *25* for 25–32 µm, *10* for < 10 µm). For example, *ol300Pd45* is the experiment conducted with San Carlos olivine at 300 °C in an AgPd capsule and for an initial grain size of 45–50 µm (Table 2).

3.3 Experimental equipment

In this study, all experiments were performed in René 41 rapid-quench cold-seal pressure vessels (Rudert et al., 1976; Pichavant, 1987; Schmidt et al., 1995) pressurized with Ar. Experimental temperatures, monitored permanently with an external thermocouple, were controlled with a Eurotherm regulator. Temperatures inside the vessel were calibrated under pressure using two thermocouples (precise to ±2 °C according to the manufacturer), spaced 3 cm apart and positioned at the points occupied by the ends of the capsule. In order to minimize the thermal gradient within the capsule, the vessel was positioned in the furnace so that the temperature difference between the calibration thermocouples was less than 1 °C. Pressure was read with a tube manometer to within ±2 MPa. In this study, pressure was kept constant (50 MPa) and two temperatures, 300 and 350 °C, were investigated. Experiments lasted for 30, 45, or 80 d (Table 2). Once completed, the experiment was quenched by removing the pressure vessel from the furnace and allowing it to cool for ≈ 1 h down to room conditions. When cold, the vessel was opened and the capsule extracted. It was cut parallel to its long axis so that the entire sample volume was exposed and recovered.

3.4 Analytical methods

Compositions of the starting San Carlos olivine and the starting olivine and orthopyroxene of the Åheim dunite have been determined with a Cameca SX Five electron microprobe (ISTO, Orléans). Analyses were carried out in punctual mode using a 15 kV acceleration voltage, a 6 nA sample current, and a 10 and 5 s acquisition time on peak and background respectively. Solid products recovered after the experiments were dried at 110 °C for 24 h. A fraction was ground and mounted in a capillary for X-ray diffraction (XRD) analysis. An Inel CPS120 diffractometer equipped with a curved detector and a Co anticathode was used (ISTO, Orléans). Magnetic data including hysteresis parameters (saturation magnetization: J_s; saturation remanent magnetization: J_{rs}; intrinsic coercivity: H_c; remanent coercivity: H_{cr}) were obtained using a vibrating sample magnetometer at room temperature (MC MicroMag 3900 Series, IPGP Paris). The magnetite mass fraction (MMF) was obtained using the calibration between the amount of magnetite and J_s (proportionality factor of 92 $A\,m^2\,kg^{-1}$ determined from powder mixtures made of synthetic forsterite and magnetite; Malvoisin et al., 2012b). Progress of the serpentinization reaction was calculated from the amount of magnetite produced (MMF) using model 3 of (Malvoisin et al., 2012b). Another fraction of experimental products was selected for detailed textural characterization and phase identification using scanning electron microscopy (SEM) and Raman micro-spectroscopy. Run products were either embedded in epoxy and polished or directly glued on a glass plate. The SEM of the joint BRGM-ISTO facility (Tescan Mira 3 XMU, ISTO Orléans) was used both in secondary (SE) and back-scattered electron (BSE) modes. To reduce charging effects, samples were sputtered with carbon before analysis. Raman characterization of oxides was performed using a Jobin-Yvon Labram HR800 Raman spectrometer (LPG, Nantes) equipped with a CCD detector, a 532 nm solid-state laser, a 1800 grooves mm^{-1} grating, and a 100× Olympus objective in confocal mode. Acquisition times were 5×60 s. To avoid oxide deterioration (de Faria et al., 1997), the laser beam power was optimized on magnetite and hematite powders provided by Sigma Aldrich and comparable in size to those observed in our synthesized products. Thus, a laser power output set at 50 mW (corresponding

to 1.5 mW at sample level) was used in conjunction with a filter reducing the laser power by a factor 10. Raman spectra of iron oxides could be acquired only on samples with the largest grain sizes, after pre-localization of iron oxides using SEM images.

Iron oxide characterization (nature and proportion) was carried out by coupling four methods: SEM, XRD, Raman micro-spectroscopy, and magnetic properties. SEM informed on the presence of iron oxides and on textural relations with other phases and provided a relative quantification of their abundances in the samples. Identification of hematite was based on XRD and Raman data. The distinction between magnetite and maghemite ($\gamma Fe_2^{3+}O_3$), while being ambiguous from XRD (Malvoisin et al., 2012b), was achieved from the Raman data, whereas the magnetic properties, in particular the J_s measurements, allowed quantification of amounts of magnetite or maghemite present.

Due to the low serpentine abundances and the similarities between XRD spectra of chrysotile and lizardite, it was not possible to clearly discriminate between the different serpentine polymorphs by this method. In contrast to iron oxides, attempts to characterize serpentine polymorphs by Raman spectroscopy (Lemaire, 2000; Auzende et al., 2004; Schwartz et al., 2013; Rouméjon et al., 2015) were inconclusive, and the identification of these polymorphs in this study is based on textural parameters, notably the characteristic acicular habit (fibrous texture) of the chrysotile.

4 Results

4.1 San Carlos olivine

Fourteen experiments, half in Au and half in AgPd and covering a range of initial grain sizes, durations, and temperatures are reported in Table 2.

4.1.1 Textures

Textures of experimental products are illustrated in Fig. 2. For the coarser initial grain sizes (0.5–1 mm), serpentinization products are concentrated within the starting olivine crystals, in large veins (Fig. 2a and b) or gulfs (Fig. 2c) rather than at its free surface. Vein widths are approximately 5 µm, and two different vein types can be distinguished from SEM observations on orthogonal sections. The first type is mainly composed of fibrous material, interpreted to be chrysotile (see Sect. 3.4). Iron oxides occur as small crystals irregularly dispersed along the vein. The vein is not completely filled by product phases, and there is a void between olivine and the material crystallized in the vein (Fig. 2a). The second type, only observed in Au capsules, is texturally similar to the first, being also symmetrical with respect to the center of the vein. It comprises chrysotile and iron oxides, but the fibrous phase displays a contrast difference: lighter near the olivine and darker in the center of the vein. As for the first type, a void is observed between the light band and olivine (Fig. 2b). Whatever the type of vein, iron oxides are almost always sandwiched between olivine and serpentine (Fig. 2a and b). This textural relationship between minerals is also observed in dissolution gulfs present at the surface of the crystals (Fig. 2c). An extensive search for brucite in the veins with SEM and Raman proved negative.

For smaller initial grain sizes, fibrous chrysotile develops on the surface of the residual olivine crystals where it forms a 5 µm layer (Fig. 2d and e). Olivine can be completely rimmed by serpentine (Fig. 2f). Other reaction products include iron oxides, present locally in very different proportions and sizes (Fig. 2d and g). Brucite is absent.

4.1.2 Mineral assemblages

Olivine, detected by XRD in all charges, persists in all experimental products (Table 2). Similarly, serpentine and iron oxides are present in all experimental charges on the basis of SEM observations (Fig. 2), although they are detected by XRD in only a few experiments (Table 2). Serpentine is detected by XRD in all charges with the smallest initial grain sizes (10 µm) and in only one with an intermediate initial grain size (*ol300Pd45*; Fig. 3, Table 2). It coexists on XRD patterns with iron oxides in most charges (*ol300Pd45*, *ol300Au10*, *ol300Pd10* at 300 °C; *ol350Pd10* at 350 °C) and is more rarely found in isolation (*ol350Au10* at 350 °C; Fig. 3, Table 2). Examination of XRD patterns suggest that serpentine is produced in generally small amounts, except in *ol300Pd10* (Fig. 3). Despite extensive tracking with SEM using EDS (energy-dispersive X-ray spectroscopy) and WDS (wavelength-dispersive spectrometry) element maps, brucite was not found and must be considered as absent from San Carlos charges.

Experimental iron oxide products include magnetite and hematite. Magnetite was positively identified by Raman in the four experiments with coarse initial grain sizes, performed both in Au (*ol300AuG*, *ol350AuG*) and AgPd (*ol300PdG*, *ol350PdG*; Fig. 4, Table 2). Maghemite (spectrum characterized by a doublet at 665 and 621 cm^{-1}, Legodi and de Waal, 2007, Fig. 4) was not found despite extensive search. In experiments performed with small initial grain sizes in Au at 300 °C (*ol300Au10*) and in AgPd at 350 °C (*ol350Pd10*), the iron oxide peaks at 35.13° 2θ and 50.52° 2θ in XRD spectra are attributed to magnetite (Fig. 3, Table 2) because maghemite is absent in the corresponding experiments performed with large initial grain sizes (respectively *ol300AuG* and *ol350PdG*, Fig. 4). Following the same reasoning, the increase of J_s (Table 4) relative to this of the starting olivine (baselines in Fig. 5) is attributed to the presence of magnetite and allows the calculation of magnetite mass fraction (MMF) in products (Table 2). Magnetic measurements thus highlight the formation of magnetite in two supplementary samples: *ol300Au45* and *ol300Pd10* (Fig. 5a, Table 2). They are also in good agreement with the XRD

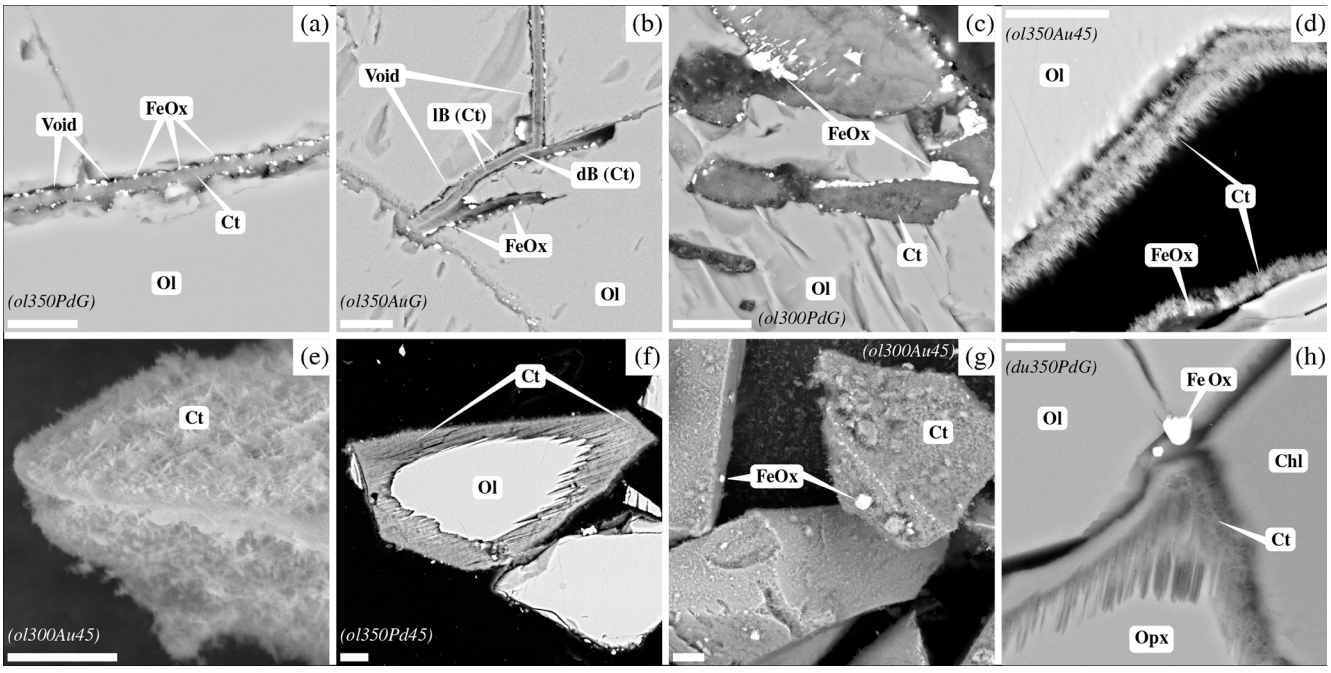

Figure 2. SEM images of reacted San Carlos olivines **(a–g)** and Åheim dunite **(h)**. For each view, the scale bar is 10 µm. Mineral abbreviations are the same as in Table 2. **(a–d, f, h)** Polished sections and **(e, g)** unpolished preparations. **(a)** Vein developed in San Carlos olivine crystal; the middle of the vein is occupied by fibrous chrysotile; iron oxides are concentrated in the void left between olivine and the chrysotile band (BSE, *ol350PdG*). **(b)** Texture similar to **(a)** except that the band is filled with chrysotile showing different contrast (light: lB and dark: dB; BSE, *ol350AuG*). **(c)** Dissolution gulf filled with large iron oxides and chrysotile (BSE, *ol300PdG*). **(d)** ≈ 5 µm thick chrysotile layer surrounding olivine crystal and containing < 1 µm iron oxides in very limited amounts (BSE, *ol350Au45*). **(e)** Fibrous texture of chrysotile (SE, *ol300Au45*). **(f)** Chrysotile layer rimming olivine crystal (*ol350Pd45*). **(g)** Chrysotile and numerous iron oxides with sizes up to 5 µm developed on the surface of olivine crystals (BSE, *ol300Au45*). **(h)** BSE image of dunite reacted in AgPd capsule (*du350PdG*). Orthopyroxene is more markedly dissolved than olivine. The iron oxide is most probably maghemite (see text). The fibrous material developed at the grain interface is chrysotile.

measurements since the two samples with the highest MMF are those for which magnetite is detected by XDR (Fig. 3, Table 2). Magnetite is thus confirmed in eight charges, half in Au half in AgPd, while it forms preferentially at 300 rather than 350 °C (five vs. three occurrences, respectively).

Hematite was identified by Raman in three of the four coarse-grained samples analyzed (*ol300PdG*, *ol350AuG*, *ol350PdG*; Fig. 4, Table 2) and by XRD in three charges: two with the smallest initial grain sizes (*ol300Pd10*, *ol350Pd10*) and, only one, same as for the serpentine, with intermediate initial grain sizes (*ol300Pd45*; Fig. 3, Table 2). Hematite is preferentially associated with the AgPd experiments. It is absent in Au at 300 °C (*ol300AuG*) but present in the corresponding charge at 350 °C (*ol350AuG*; Fig. 4, Table 2). A total of six charges, half at 300 °C and half at 350 °C, contain hematite.

4.1.3 Magnetic properties

The hysteresis data for experimental products (Table 4) are plotted in a J_{rs}/J_s vs. H_{cr}/H_c diagram (Day diagram; Fig. 6, Day et al., 1977) where J_{rs}/J_s is the ratio of saturation remanent magnetization to saturation magnetization and H_{cr}/H_c the ratio remanent coercivity to intrinsic coercivity. The Day diagram is a useful way to discriminate between various magnetic mineralogies and grain sizes using magnetization and coercivity parameters (Dunlop, 2002; Malvoisin et al., 2012b). For magnetite, the single-domain (SD, $J_{rs}/J_s > 0.5$ and $H_{cr}/H_c \approx 1$, Fig. 6) corresponds to particle sizes smaller than ≈ 0.05–0.08 µm, while the multidomain (MD; $J_{rs}/J_s < 0.05$ and $H_{cr}/H_c > 4$, Fig. 6) is reached for magnetite particles larger than 3–15 µm (Oufi et al., 2002). Between these two grain sizes, the magnetic properties evolve in the pseudo-single-domain (PSD) transition zone. The magnetic properties of our experimental samples (only those with MMF above the baselines; see Fig. 5) are compared with those from other experimental studies and natural serpentinites from the literature. All our experimental magnetites plot in the PSD field (Fig. 6). Magnetites produced in Au capsules at 300 °C are in good agreement, in terms of J_{rs}/J_s, with other experimental magnetites at 300 °C (Malvoisin et al., 2012b), although the latter extend to higher H_{cr}/H_c values (Fig. 6). Magnetites from AgPd have systematically higher J_{rs}/J_s than magnetites from Au capsules (Fig. 6). Taken together,

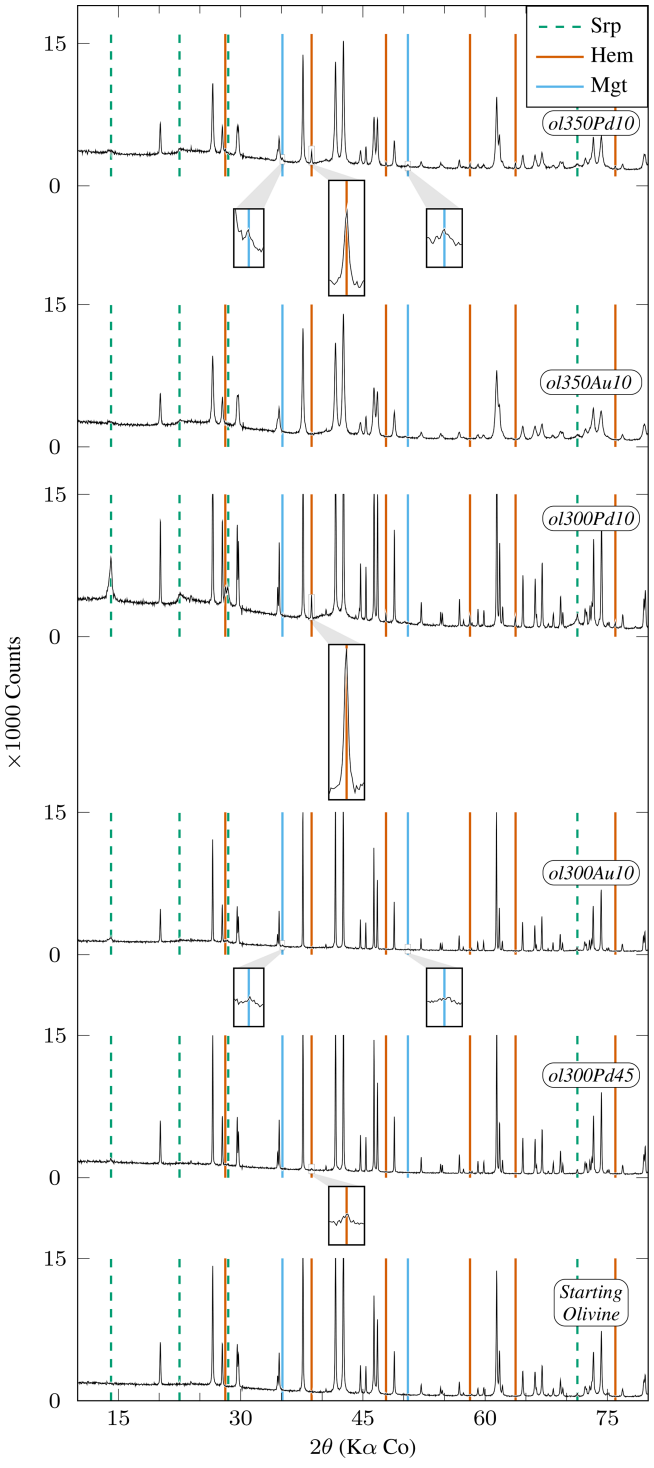

Figure 3. XRD diffractograms of experimental charges produced from San Carlos olivine emphasizing phases other than primary olivine (Table 2). Mineral abbreviations are the same as in Table 2. Peaks which are not highlighted correspond to olivine. All peaks higher than 15 000 counts are clipped. Insets are ×6 magnifications of diffractograms. San Carlos olivine is still present at the end of all experiments. Relative olivine and serpentine peak intensities demonstrate limited formation of serpentine except in *ol300Pd10*. *ol300Pd45* is the only charge with initial grain size > 10 µm showing detectable serpentine and hematite peaks (inset centered on the 38.71° 2θ peak). Relative peak intensities suggest a more advanced reaction in *ol300Pd10* (< 10 µm initial grain size) than in *ol300Pd45* (45–50 µm). Hematite is identified in experiments performed in AgPd capsules (*ol300Pd10*, *ol350Pd10*, and *ol300Pd45*). Peaks observed in *ol350Pd10* and *ol300Au10* at 35.13° 2θ and 50.52° 2θ (insets) are attributed to magnetite (see text).

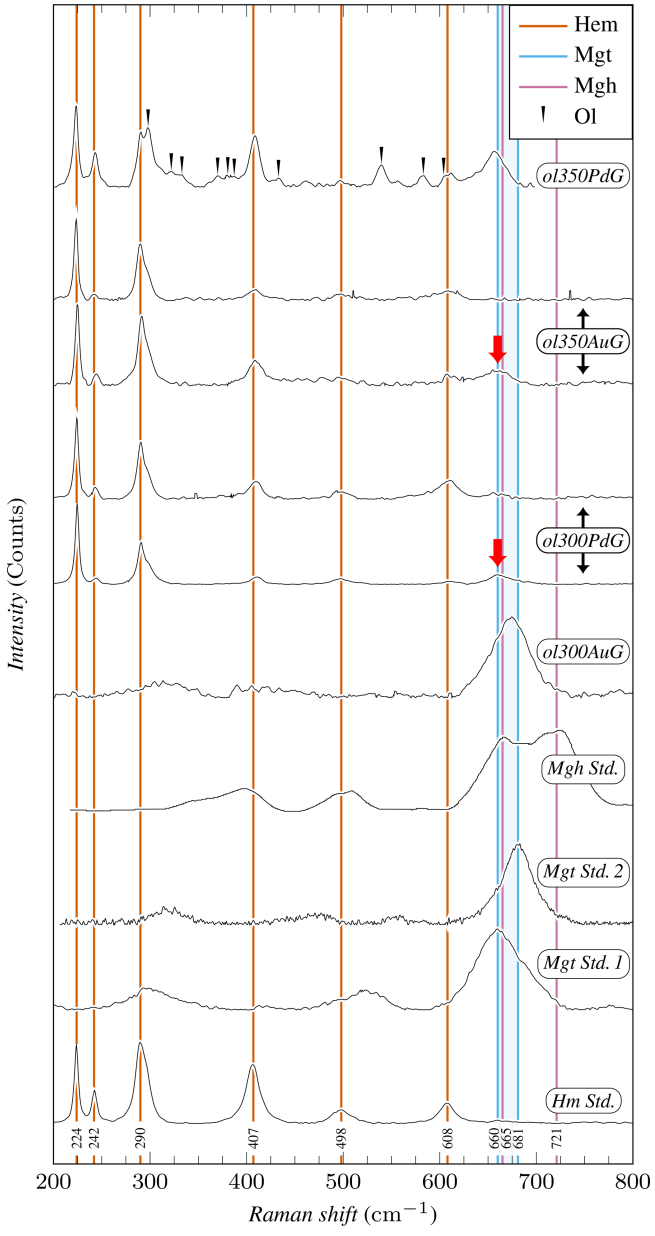

Figure 4. Representative Raman spectra of iron oxides. Raman spectra have been normalized to 1 based on the maximum intensity recorded for each spectrum. Mineral abbreviations are the same as in Table 2. *Hm Std.* and *Mgt Std. 1* spectra have been acquired on hematite and magnetite standard powders, respectively. *Mgt Std. 2* spectrum corresponds to the R061111 magnetite sample from the RRUFF database (rruff.info, 2023), while maghemite standard (*Mgh Std.*) comes from Legodi and de Waal (2007). Maghemite is characterized by a doublet at 665 and 621 cm^{-1}, while magnetite is characterized by a single peak in the 660–681 cm^{-1} range (the area colored in blue delimits the magnetite peak position in *Mgt Std.1* and *Mgt Std. 2*). None of the samples studied contains maghemite, while magnetite is present in *ol300AuG* and *ol350PdG* and also in lesser amounts in *ol300PdG* and *ol350AuG* (red arrows). Except in *ol300AuG*, hematite is clearly identified in the three other samples.

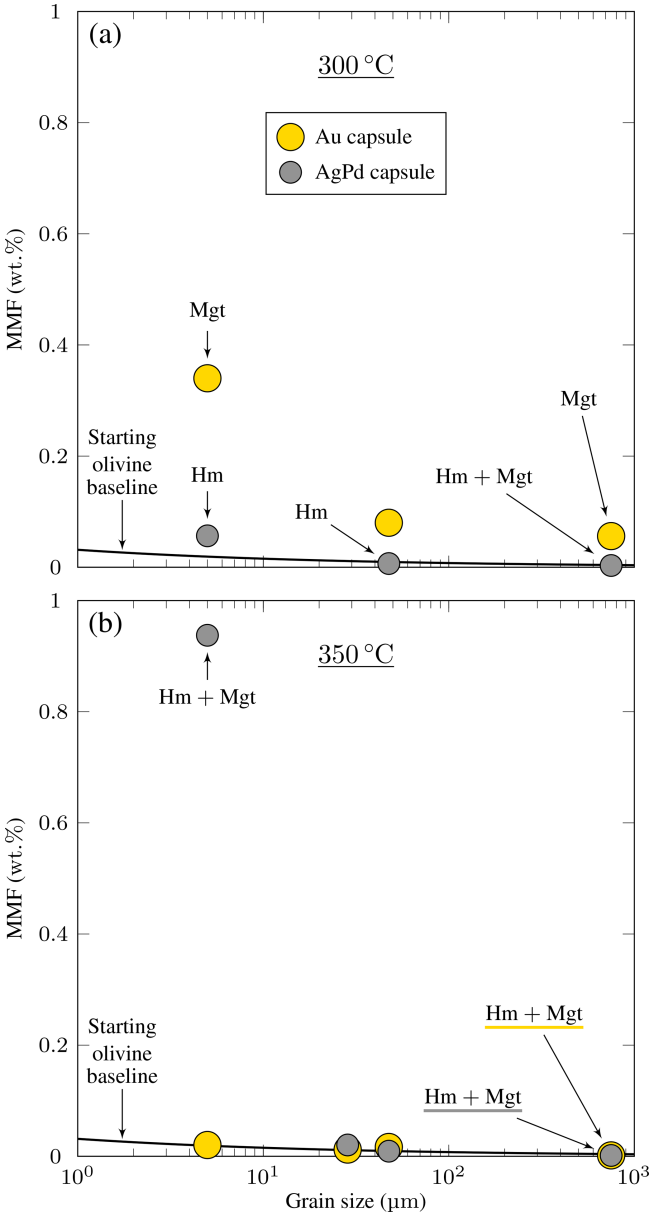

Figure 5. Amounts of magnetite in reaction products (magnetite mass fraction, MMF, Table 2) plotted against the initial grain size for the San Carlos olivine experiments. Experiments are distinguished by capsule material, either Au or AgPd. The method for constructing the starting olivine baseline is detailed in Appendix C. Hm and Mgt correspond to hematite and magnetite, respectively. **(a)** 300 °C charges. Note the systematic increase of MMF with decreasing grain size observed in experiments with Au capsules. Experiments with AgPd capsules show a modest increase of MMF < 10 µm. **(b)** 350 °C charges. No significant increase of MMF is observed except for the experiment carried out with the smallest initial grain size in AgPd capsule (*ol350Pd10*).

Table 4. Hysteresis measurements.

Experiment	J_s[a] ($mA\,m^2\,kg^{-1}$)	J_{rs}[a] ($mA\,m^2\,kg^{-1}$)	H_c (mT)	H_{cr} (mT)
San Carlos olivine				
ol300AuG	51.54	3.90	7.60	24.62
ol300PdG	2.87	0.35	14.32	35.98
ol300Au45	73.63	6.43	8.90	29.11
ol300Pd45	6.10	1.07	11.07	29.10
ol300Au10	312.83	27.79	10.76	35.30
ol300Pd10	51.99	6.85	10.72	33.90
ol350AuG	1.51	0.15	9.91	21.94
ol350PdG	1.35	0.13	3.90	na[b]
ol350Au45	15.42	2.33	11.55	25.87
ol350Pd45	8.45	0.40	4.40	19.75
ol350Au25	11.15	1.36	8.63	19.21
ol350Pd25	18.75	0.85	4.15	8.26
ol350Au10	18.67	3.72	14.88	33.63
ol350Pd10	862.53	135.11	11.33	28.01
Åheim dunite				
du350AuG	9.62	2.52	18.25	35.10
du350PdG	27.74	8.23	22.10	39.21

[a] J_s and J_{rs} are weighted by the analyzed sample mass. [b] na: not analyzed.

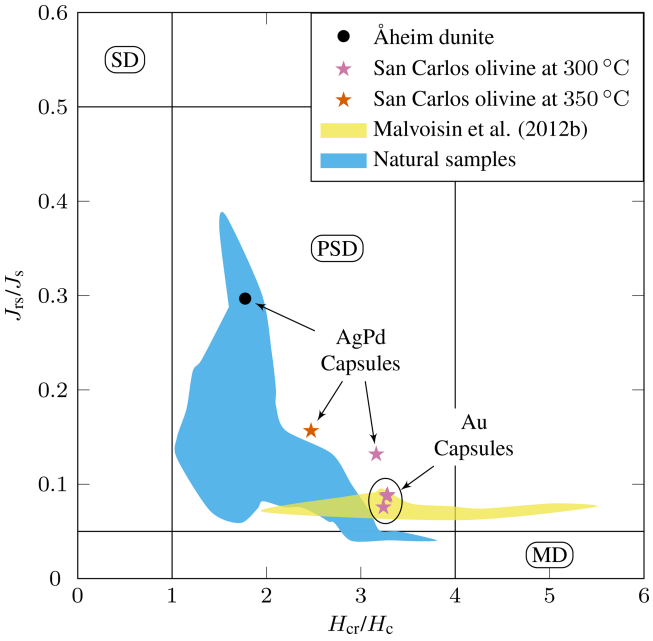

Figure 6. J_{rs}/J_s as a function of H_{cr}/H_c plot (Day diagram, Day et al., 1977) for selected experimental products. Only charges with magnetite mass fractions (MMFs) higher than the baseline (see Fig. 5) and thus containing a substantial amount of magnetite are plotted. SD: single domain, PSD: pseudo single domain, and MD: multi domain. The yellow field corresponds to the experiments of Malvoisin et al. (2012b) on San Carlos olivine plus pure water at 300 °C. The blue field corresponds to natural serpentinite samples (DSDP Sites 395, 556, 558, and 560 and ODP Sites 670, 895, and 920, as compiled by Oufi et al., 2002).

the experimental magnetites follow a trend broadly similar to that of magnetites from natural systems (Oufi et al., 2002), although, for a given H_{cr}/H_c, the experimental magnetites plot at higher J_{rs}/J_s than the natural (Fig. 6).

4.1.4 Influence of capsule material, temperature, and grain size

All 300 °C charges contain serpentine and iron oxides irrespective of the capsule material. However, charge *ol300Pd10* has the strongest serpentine XRD signal in our sample set (Fig. 3). In comparison, serpentine is only present in small amounts in the 350 °C charges, whether performed in Au or AgPd (*ol350Au10*, *ol350Pd10*, Fig. 3). Therefore, the data suggest a decrease in serpentine production upon increasing temperature from 300 to 350 °C and a higher serpentine production in AgPd than in Au at 300 °C. This latter statement is supported by the XRD detection of serpentine for intermediate grain sizes only in AgPd (*ol300Pd45*; Fig. 3), although in smaller amounts than for *ol300Pd10*. We conclude that serpentine preferentially forms at 300 °C in AgPd capsules and in experiments performed with small initial grain sizes.

A first-order change in the nature of the iron oxide phase is observed between the Au and the AgPd experiments at 300 °C. The former contains magnetite and the latter hematite, although a small amount of magnetite is present together with hematite in *ol300PdG* and *ol300Pd10* (Figs. 4, 5, Table 2). This subdivision between Au and AgPd experiments is less strongly marked at 350 °C since hematite coexists with magnetite in *ol350AuG*, *ol350PdG*, and *ol350Pd10*, but magnetite is present in low amounts in *ol350AuG* (Fig. 4, Table 2). SEM observations show that iron oxides are generally more abundant and grow bigger at 300 °C (up to 5 µm) than at 350 °C ($\leq$ 1 µm; Fig. 2a–d and g), consistent with the evolution of magnetic properties with increasing temperature. At 350 °C, magnetite has a lower H_{cr}/H_c and higher J_{rs}/J_s than at 300 °C, which indicates a trend toward the SD field and thus smaller grain sizes (Fig. 6). The magnetite production increases with decreasing grain size at 300 °C in Au (Fig. 5a, Table 2). The same type of evolution is observed in AgPd, although the low MMFs (Fig. 5a) indicate that magnetite production is much more limited than in Au. In comparison, at 350 °C, no such increase of the MMF is observed in Au (Fig. 5b and Table 2) and iron oxides occur in amounts insufficient to be detected by XRD (Table 2). In *ol350AuG*, the Raman data show that hematite is the predominant iron oxide and that magnetite is present only in small amounts (Fig. 4). MMFs are also low in AgPd at 350 °C (Fig. 5b), indicating a very limited magnetite production at the exception of the charge performed with the smallest grain size (*ol350Pd10*; Table 2), discussed separately below. We conclude that magnetite preferentially forms at 300 °C in Au

rather than in AgPd and in experiments performed with small initial grain sizes.

Hematite is encountered in all 300 and two 350 °C experiments performed in AgPd and in only one in Au at 350 °C (*ol350AuG*; Figs. 3, 4, Table 2). Relative XRD peak intensities in *ol300Pd45* and *ol300Pd10* (Fig. 3) imply that hematite production increases with decreasing initial grain size. At 350 °C (*ol350Pd45*), hematite is not detected by XRD at the difference of at 300 °C (*ol300Pd45*) for the same initial grain size (Fig. 3, Table 2), indicating a decrease in hematite production from 300 to 350 °C. We conclude that hematite preferentially forms at 300 °C in AgPd capsules and in experiments performed with small initial grain sizes.

Charge *ol350Pd10* (Table 2) combines the presence of iron oxides in amounts sufficient to be detected by XRD (Fig. 3), a very high J_s (the highest of the entire dataset, Table 4), and a relatively small serpentine production (Fig. 3). Hematite is detected by XRD (Fig. 3), and the other iron oxide in the pattern is interpreted to be magnetite since magnetite (but not maghemite) has been identified in the Raman spectra of the corresponding coarse-grained charge (*ol350PdG*; Fig. 4). Thus, the strong J_s implies a very high MMF, in fact the highest MMF in our sample set (Fig. 5b, Table 2). This indicates an exceptionally high magnetite production in this 350 °C AgPd charge performed with the smallest initial grain size.

4.2 Åheim dunite

Two experiments are available, each for internal and external control of f_{H_2} (i.e., Au and AgPd capsules respectively) at 350 °C for similar durations (≈ 1050 h) and on a relatively coarse-grained starting material (≈ 2000 µm; Table 2). Both olivine and orthopyroxene persist in experimental products, although orthopyroxene appears more reacted. The XRD data indicate that the relative proportions of orthopyroxene decrease more markedly than olivine (Fig. 7), and dissolution textures are more clearly marked on orthopyroxene than on olivine (Fig. 2h). Serpentine appears only as fibrous chrysotile (Fig. 2h), while brucite was not found. In the Au capsules, no iron oxide could be detected either by XRD or SEM, consistent with the MMF being only slightly higher than in the starting material (2.5×10^{-3} wt %; see Sect. 3.1 and Table 2). In contrast, AgPd capsule products contain an iron oxide phase detected by SEM (Fig. 2h). This iron oxide is probably responsible for the weak peaks observed on the XRD pattern (Fig. 7). No reliable Raman analysis could be obtained for this oxide, tentatively interpreted to be maghemite according to XRD pattern, knowing that this method does not allow magnetite to be clearly excluded (see Sect. 3.4). It occurs either in isolation or associated with Fe–Ni sulfides and in fractures or at grain boundaries. The measured MMF is substantially higher than in the Au capsule charge (Table 2), being also 1 order of magnitude higher than the starting material. Using a proportionality factor for maghemite of 78 A m^2 kg^{-1} (Cullity, 1972), the increase

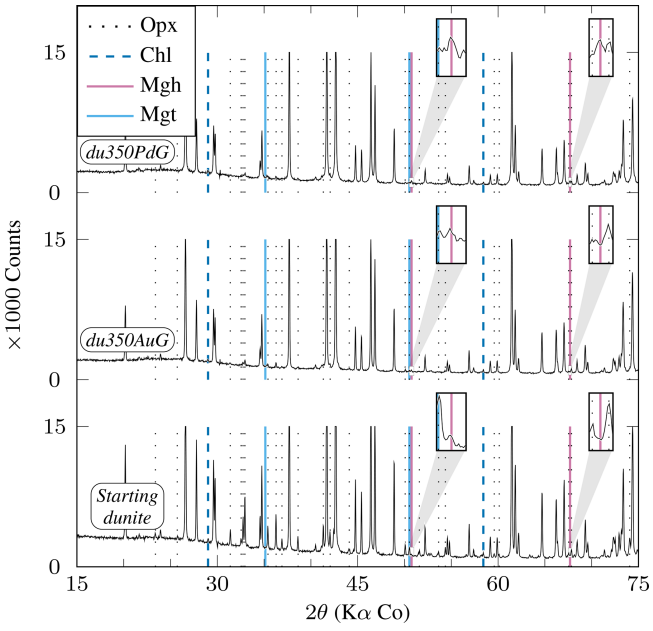

Figure 7. XRD diffractograms of experimental charges produced from Åheim dunite (Table 2). Mineral abbreviations are the same as in Table 2. Peaks which are not highlighted correspond to olivine. All peaks higher than 15 000 counts are clipped. Relative peak intensities demonstrate that orthopyroxene reacts preferentially than olivine. Insets are ×6 magnifications of diffractograms centered on the 50.76° 2θ and 67.67° 2θ peaks which highlight the presence of iron oxide in *du350PdG* consistent with the presence of maghemite (see text).

in J_s is compatible with a nominal weight of maghemite of 0.036 wt % (0.030 wt % if the iron oxide phase is magnetite). The possible occurrence of maghemite in the Åheim dunite experiment carried out in AgPd capsules is consistent with the preferential formation of hematite in the San Carlos olivine experiments carried out in AgPd. However, the cause of the polymorph change ($\alpha Fe_2^{3+}O_3$ for hematite vs. $\gamma Fe_2^{3+}O_3$ for maghemite) remains to be clarified.

5 Discussion

5.1 Control of redox conditions in the experiments

Results from this study directly depend on the reliability of our methods to control the experimental redox conditions. First, it is necessary that the H_2 generated by the serpentinization reaction remains confined within the Au capsule to sustain a reduced environment throughout the entire duration of the experiment. This necessitates that hydrogen loss (by permeation through the capsule, Harvie et al., 1980) is of negligible importance, despite our relatively long experimental durations. Second, H_2 must escape rapidly out of the AgPd capsule so that oxidized redox conditions, controlled by the Ar pressurizing medium, are imposed to the charge.

Below, we summarize the evidence confirming that both conditions were fulfilled in our experiments.

In experiments performed with Au capsules, the negligible importance of hydrogen loss is demonstrated by the following arguments:

1. Among noble metals used as capsules, hydrogen permeabilities are the lowest for Au (Chou, 1986; Gunter et al., 1987).

2. Au has been classically considered to be almost impermeable to hydrogen at low to medium temperatures, being used as the external container in double capsule assemblies used to control experimental redox states (Eugster, 1957). The permeation of hydrogen in Au is usually considered negligible below 400–450 °C (see Fig. 3 in Chou, 1986).

3. Hydrogen permeation rates have been calculated with equation 10 in Harvie et al. (1980) using Au permeability coefficients from Chou (1986) as given in Gunter et al. (1987). At 300 °C, for our capsule geometry (length: 35 mm, internal diameter: 4.6 mm, wall thickness: 0.2 mm; see above), external and internal f_{H_2} of 2.1×10^{-4} and 4.78 MPa respectively (Table 3), and an experimental duration of 80 d (1920 h, corresponding to the durations of our longest experiments, Table 2), a mass of 0.3 µg H_2 is lost. This corresponds to < 1 % of the total H_2 present for capsules loaded with 100–150 mg water (Table 2). At 350 °C, the calculated hydrogen loss reaches 1 %–2 % of the total H_2 present. These hydrogen losses are negligible.

4. No time-dependent hydrogen loss is apparent in our experimental results. At 300 °C, magnetite alone is present in all Au experiments, whether relatively long (*ol300AuG*, 2010 h) or short (*ol300Au45* and *ol300Au10*, both $\approx$ 720 h; Table 2).

5. Experiments from the literature confirm the impermeability of Au with respect to hydrogen.

   Malvoisin et al. (2012a, b) have performed serpentinization experiments of San Carlos olivine at 250–350 °C, 50 MPa for durations up to 514 d. Au capsules of 0.2 mm wall thickness and an Ar pressurizing medium were used, same as in this study. The experimental products include magnetite only, hematite being absent. Thus, there is no indication for significant hydrogen loss and for a progressive evolution towards oxidizing conditions in those experiments.

For experiments performed in AgPd capsules, the following arguments suggest that oxidized redox conditions were rapidly imposed:

1. A large contrast in hydrogen permeability constants exists between Au on the one hand and AgPd alloys on the other hand. Hydrogen permeabilities in $Ag_{25}Pd_{75}$ alloys are 8–9 orders of magnitude higher than in Au, being also higher than in pure Pd (Chou, 1986; Gunter et al., 1987).

2. Magnetite is oxidized to hematite in the *A1* test experiment performed at 350 °C (Table B1 in Appendix B). In the *A4* hydrogen sensor experiment, the determined f_{H_2} (0.9×10^{-4} MPa) is lower than that of the HM buffer (Table B1). Therefore, redox conditions more oxidizing than the HM buffer are recorded in the AgPd experiments at 350 °C and also presumably at 300 °C since f_{H_2} varies little with temperature under strongly oxidizing conditions.

3. Hydrogen permeation rates for $Ag_{25}Pd_{75}$ capsules have been calculated under conditions same as above using permeability coefficients from Gunter et al. (1987). Hydrogen transfer from inside to outside the capsule is extremely fast. For external and internal f_{H_2} of 2.1×10^{-4} and 4.78 MPa respectively, all the H_2 present inside the capsule is lost in less than 1 min. Durations of hydrogen transfer vary with the internal f_{H_2} but remain extremely short. Therefore, $Ag_{25}Pd_{75}$ capsules cannot keep a high internal f_{H_2} for a long time if placed in a low-f_{H_2} external environment (Ar pressure medium), and oxidized conditions are almost instantaneously imposed to the charge.

5.2 Reaction mechanisms

5.2.1 Serpentinization

Serpentine appears in all product phase assemblages from this study (with the exception of the Åheim dunite charge in Au), and this demonstrates that a serpentinization reaction takes place in the experiments. Several serpentine-forming reactions have been proposed in the literature (Seyfried et al., 2007; Marcaillou et al., 2011; Okamoto et al., 2011; Malvoisin et al., 2012a, b; McCollom et al., 2016; Fauguerolles, 2016; Lamadrid et al., 2017; Huang et al., 2017a). The general mechanism can be conveniently described by the following global reaction:

$$\underset{\text{Olivine(Fo}_{91})}{(Mg_{0.91}Fe_{0.09})_2SiO_4} + \alpha H_2O \rightarrow \underset{\text{Serpentine}}{\beta(Mg, Fe^{2+}, Fe^{3+})_3(Si, Fe^{3+})_2O_5(OH)_4} + \underset{\text{Brucite}}{\gamma(Mg, Fe^{2+})(OH)_2} + \delta \underset{\text{Magnetite}}{Fe^{2+}Fe_2^{3+}O_4} + \epsilon H_2, \quad \text{(R3)}$$

which emphasizes that serpentine, brucite, and magnetite are the main product phases of the reaction. The α, β, γ, δ, and ϵ coefficients in Reaction (R3) depend in detail of the composition of reaction products and of the partitioning of Fe^{2+} and Fe^{3+} between product phases.

Our experimental results under conditions of internal f_{H_2} control (Au capsule experiments) at 300 °C are broadly consistent with Reaction (R3). Olivine is consumed, and both serpentine and magnetite are produced (*ol300AuG*, *ol300Au45*, *ol300Au10*; Table 2). However, brucite is not present in our charges (whatever the granulometry of the starting material), in contrast with what is expected from Reaction (R3). In comparison, we note that Malvoisin et al. (2012a) reported brucite in their experiments performed under the same conditions (Au capsules and temperatures) and with the same starting material (San Carlos olivine). Several explanations have been proposed for the absence of brucite in experimental and natural serpentinites. For example, a mechanism based on precipitation of carbonates could account for the absence of brucite (Kelemen and Matter, 2008), but it is irrelevant in our case since our experimental products contain no carbonate phase. High aqueous silica activities ($a_{SiO_2(aq)}$) imposed by dissolution of local orthopyroxene or inherited by the fluids from previous encountered lithologies may also explain the absence of brucite (Frost and Beard, 2007; Frost et al., 2013; Tutolo et al., 2018). This mechanism could account for the lack of brucite in the Åheim dunite but not in the San Carlos experiments. However, contamination of silica from the agate mortar during preparation of the starting olivine powders is a possibility.

According to Reaction (R3), serpentinization of Fo_{91} (Mg# = 0.91) olivine yields serpentine with Mg# > 91 coexisting with brucite with Mg# < 91 (Bach et al., 2006; Malvoisin et al., 2012a; Klein et al., 2013). The distribution of Mg and Fe between serpentine and brucite determines the amount of "free" Fe which is mobilized as magnetite. For example, for the serpentine–magnetite assemblage, the Mg# of serpentine increases with increasing f_{O_2} (decreasing f_{H_2}) and decreasing $a_{SiO_2(aq)}$ (Frost et al., 2013) according to the following reaction:

$$\underset{\text{Serpentine(Mg\#=0.92)}}{(Mg_{0.92},Fe_{0.08})_3Si_2O_5(OH)_4} \rightleftharpoons \frac{1}{24}\underset{\text{Serpentine(Mg\#=0.96)}}{(Mg_{0.96},Fe_{0.04})_3Si_2O_5(OH)_4} + \frac{1}{24}\underset{\text{Magnetite}}{Fe_3O_4} + \frac{1}{24}H_2O + \frac{1}{24}H_2 + \frac{1}{12}SiO_2(aq), \quad \text{(R4)}$$

where the incorporation of Fe^{3+} in serpentine (Seyfried et al., 2007; Marcaillou et al., 2011; Andreani et al., 2013) is not considered. The transition from a serpentine–magnetite to a serpentine–brucite assemblage marks a decrease in f_{O_2} (or increase in f_{H_2}) at constant $a_{SiO_2(aq)}$ (Frost et al., 2013) and could be depicted by the following reaction:

$$\underset{\text{Serpentine(Mg\#=0.96)}}{(Mg_{0.96},Fe_{0.04})_3Si_2O_5(OH)_4} + \frac{1}{20}\underset{\text{Magnetite}}{Fe_3O_4} + \frac{1}{10}H_2O + \frac{1}{20}H_2 \rightleftharpoons \underset{\text{Serpentine(Mg\#=0.92)}}{(Mg_{0.92},Fe_{0.08})_3Si_2O_5(OH)_4} + \frac{3}{20}\underset{\text{Brucite}}{(Mg_{0.80},Fe_{0.20})(OH)_2}. \quad \text{(R5)}$$

Thus, a serpentine–magnetite assemblage is indicative of conditions more oxidizing than a serpentine–brucite assemblage. In our internally controlled experiments, H_2 accumulation in the Au capsule is accompanied by an increase in f_{H_2} (and a decrease in f_{O_2}). However, because serpentine production is small in our experiments (see Sect. 5.2.2), f_{H_2} did not increase (and f_{O_2} did not decrease) sufficiently for the stabilization of a serpentine–brucite assemblage, and the system remained within the serpentine–magnetite domain in terms of f_{O_2} and $a_{SiO_2(aq)}$. A similar type of interpretation was proposed by Okamoto et al. (2011), who observed the appearance of brucite only after ≈ 500 h in hydration experiments of olivine plus water at 250 °C vapor-saturated. The late formation of brucite was attributed to a progressive evolution of the fluid from early oxidizing (i.e., sulfate reduction consumes H_2) to more reducing (serpentinization leads to H_2 accumulation) conditions during the experiments (Okamoto et al., 2011). For lower f_{H_2} (and higher f_{O_2}) as in the externally controlled experiments in AgPd, the appearance of brucite would be even more unlikely, although we recognize that the $a_{SiO_2(aq)}$ also comes into play (see Godard et al., 2013). The presence of brucite in the experiments of Malvoisin et al. (2012b, a) could reflect conditions more reducing (higher f_{H_2}) than in our internally controlled experiments, which could have been promoted by globally higher serpentine production and lower W/R ratios (up to 5 times lower) than in this study. Indeed, a lower W/R ratio implies, for identical amounts of Fe^{2+} oxidized into Fe^{3+} and consequently for identical amounts of produced H_2, a higher concentration of H_2 and so a higher f_{H_2} (Klein et al., 2013). At 350 °C, the absence of brucite is less surprising since it is actually not predicted to form at the expense of Fo_{90}, only small amounts of serpentine and trivial amounts of magnetite being expected (Klein et al., 2009, 2013).

Reaction (R4) can also be applied to explain the banded texture of reaction products in veins within the San Carlos olivines (Fig. 2b). This texture is interpreted as a chemical zonation between an early relatively Mg-rich (dark part) and a later Fe-rich (light part) serpentine. According to Reaction (R4), the transition from the dark to the light part would be explained by growth of serpentine under more reducing (higher f_{H_2}) and/or higher $a_{SiO_2(aq)}$.

For conditions of external f_{H_2} control (AgPd capsules) at 300 °C, serpentine production is higher than in the Au, and the iron oxide phases correspond to hematite (*ol300PdG*, *ol300Pd45*, *ol300Pd10*), although magnetite can be still

present (*ol300PdG* and *ol300Pd10*; Fig. 5a, Table 2). Thus, Reaction (R3) can be rewritten as

$$\underset{\text{Olivine(Fo}_{91})}{(Mg_{0.91}Fe_{0.09})_2SiO_4} + \alpha H_2O \rightarrow \underset{\text{Serpentine}}{\beta(Mg, Fe^{2+}, Fe^{3+})_3(Si, Fe^{3+})_2O_5(OH)_4} + \underset{\text{Brucite}}{\gamma(Mg, Fe^{2+})(OH)_2} + \underset{\text{Hematite}}{\delta Fe_2O_3} + \epsilon H_2. \quad \text{(R6)}$$

Reaction (R6) can be viewed as the combination of Reaction (R3) with the following reaction:

$$\underset{\text{Magnetite}}{Fe_3O_4} + \frac{1}{2}H_2O \rightleftharpoons \frac{3}{2}\underset{\text{Hematite}}{Fe_2O_3} + \frac{1}{2}H_2, \quad \text{(R7)}$$

which is the HM oxygen buffer reaction. It shows that, with hematite instead of magnetite as a product phase, the proportion of Fe^{2+} oxidized to Fe^{3+} is higher than in Reaction (R3). This implies in principle that more H_2 should be produced from Reaction (R6) than from Reaction (R3) (e.g., Frost, 1985). However, this conclusion needs to be confirmed in practice with the analysis of product phases in the two model Reactions (R3) and (R6). Andreani et al. (2013) have shown that, during the early stages of serpentinization, Fe^{3+}-bearing serpentine is produced and this generates more H_2 than expected from the amount of crystallized iron oxides (magnetite in their case).

5.2.2 Reaction progress

As is the case for other metasomatic processes, serpentinization is an irreversible transformation (Fonteilles, 1978). Previous experimental work has shown that serpentinization is a relatively slow reaction (Malvoisin et al., 2012a, b). Serpentine progressively forms when increasing the experimental duration, but bulk equilibrium at the scale of the whole charge (which would correspond to a 100 % reaction progress with all olivine present transformed to serpentine; see Sect. 5.2.1) is usually not reached. The advancement of the serpentinization reaction has been classically evaluated from the mass fraction of magnetite in reaction products (Oufi et al., 2002; Malvoisin et al., 2012a, b). This approach remains valid as long as magnetite is produced as the only iron oxide in the reaction. This situation occurs in our internally controlled experiments (Au capsules) at 300 °C. Using model 3 of Malvoisin et al. (2012b), which relates the amount of magnetite formed and the reaction progress (S) through the amount of water incorporated in hydrous phases (serpentine, brucite), advancements of 0.9 %, 1.3 %, and 5.4 % are obtained for *ol300AuG*, *ol300Au45*, and *ol300Au10*, respectively (Table 2). Thus, the serpentinization reaction is relatively little advanced in our 300 °C experiments, in agreement with the low amounts of serpentine in XRD spectra and the lack of brucite in experimental products. The S values demonstrate a progressive increase of reaction kinetics with decreasing initial grain size at 300 °C, although durations are not exactly the same between the three experiments (2010 h for *ol300AuG* vs. 720 h for *ol300Au45* and *ol300Au10*; Table 2). At 350 °C in Au charges, the advancement of reaction cannot be estimated because the MMFs are not systematically higher than the baseline (see Fig. 5). Furthermore, the presence of hematite (at least in *ol350AuG*) excludes the use of this method. If comparison is made for similar durations and experimental parameters, reaction advancements in our 300 °C Au experiments are significantly smaller than those observed by Malvoisin et al. (2012a). For example, for a 720 h run with an initial grain size of 38–50 µm at 300 °C, an advancement of about 6 % was measured (Run #10 in Malvoisin et al., 2012a), vs. 1.3 % in this study for a similar granulometry (*ol300Au45*, Table 2). This stresses differences in reaction kinetics between studies, although there is also a substantial intrinsic variability between experiments. As an illustration, for different runs of 720 h duration with a 5–15 µm initial grain size at 300 °C, reaction advancements cover a large range from 13 to 70 % (Runs #16 and #22, respectively, in Malvoisin et al., 2012a). In *ol300Au10* (our experiment the closest in duration and initial grain size for comparison), the advancement is 5.4 % (Table 2). This suggests the existence of rate-limiting mechanisms acting on the kinetics of the serpentinization reaction in addition to the initial granulometry. One of these mechanisms could be armoring due to precipitation of secondary phases, which limits access of the fluid to the olivine surface (Oelkers et al., 2018). This mechanism would be particularly critical if, as suggested by Malvoisin et al. (2012a), reaction kinetics are correlated to surfaces of olivine grains and the dissolution process of olivine acts as the limiting factor. Another indication for the slow serpentinization kinetics in our experiments is provided by the absence of brucite since it is symptomatic of low-f_{H_2} conditions consistent with a small serpentine production (see above and Okamoto et al., 2011).

In our externally controlled experiments (AgPd capsules), the continuous removal of H_2 from the charge toward the pressurizing medium could act to promote the advancement of the serpentinization reaction (Le Chatelier principle). Since hematite sequesters Fe, the proportion of magnetite is necessarily impacted, and models based on the production of magnetite to quantify the advancement of the serpentinization reaction are no longer applicable. However, the XRD and MMF data show that the highest production of serpentine and magnetite are reached in the externally controlled experiments (*ol300Pd10* at 300 °C and *ol350Pd10* at 350 °C, respectively). An enhanced advancement of the serpentinization reaction in externally controlled experiments is also consistent with *ol300Pd45*, the only charge with initial grain size > 10 µm having serpentine and hematite detected by XRD. The increase in serpentine proportion from *ol300Pd45* to *ol300Pd10* (Fig. 3), i.e., upon decreasing the initial grain size, is not accompanied by an increased magnetite production since MMF values remain practically un-

changed (Fig. 5a, Table 2). Therefore, in the externally controlled experiments, the advancement of the serpentinization reaction and the production of magnetite are clearly decoupled. This has important consequences for the estimation of serpentinization rates in natural oceanic systems (Cannat et al., 2010).

5.2.3 Role of temperature

Experiments performed on San Carlos olivines have demonstrated a decrease in serpentine production upon increasing temperature from 300 to 350 °C (see Sect. 4.1.4). In the same way, there is a general decrease in the MMF and magnetite production from 300 to 350 °C with the exception of one charge (*ol350Pd10*). Overall, these observations indicate that the serpentinization Reactions (R3) and (R6) are fully operative at 300 °C and much less developed at 350 °C, although serpentine is still present as indicated by results both on the Åheim dunite and the San Carlos olivines (Table 2). This has the consequence that less H_2 is generated at 350 than at 300 °C, so f_{H_2} reaches lower values in Au capsule experiments at 350 than at 300 °C, which explains the presence of hematite in *ol350AuG* (Table 2). These results are consistent with previous experimental and theoretical studies where 350 °C was found to be approximately the upper temperature limit for serpentinization (McCollom and Bach, 2009; Klein et al., 2013). Thermodynamic modeling of serpentinization reactions has shown that, for an oxidizing fluid and a high W/R ratio, the serpentine stability field can slightly exceed 350 °C; under these conditions, the magnetite proportions increase and hematite appears as a reaction product (Malvoisin, 2015; Ely et al., 2023). Therefore, our 350 °C experimental results are qualitatively consistent with these calculations, with the exception of one AgPd charge (*ol350Pd10*). This 350 °C charge is characterized by a very important iron oxide production (see Sect. 4.1.4). It has a MMF much higher than in the corresponding charge at 300 °C (*ol300Pd10*) and which also markedly exceeds that in the corresponding Au charge at 350 °C (*ol350Au10*; Fig. 5; Table 2). The increase in MMF with decreasing grain size is also very abrupt in the 350 °C AgPd experiments (Fig. 5b), thus stressing the anomalous character of the charge. Since iron oxide production in *ol350Pd10* is decoupled from serpentine formation (see Sect. 4.1.4), one possibility to be considered to explain the abnormally high magnetite production and presence of hematite is direct oxidation of olivine (e.g., Khisina et al., 1998; Knafelc et al., 2019). However, such mechanisms have been shown to work under anhydrous conditions and at temperatures generally higher than in this study. If operative at 350 °C under hydrothermal conditions, we note that olivine oxidation should be also observed in the 350 °C Au charge (*ol350Au10*), which is not the case (Fig. 5b; Table 2). Therefore, a satisfactory explanation of the *ol350Au10* charge must await further studies.

5.3 Iron oxides as redox indicators in serpentinization environments

H_2 production in serpentinization environments is coupled with the oxidation of Fe^{2+} into Fe^{3+} incorporated in serpentine and iron oxides (see Sect. 1). Among those, magnetite ($Fe^{2+}Fe^{3+}_2O_4$) is the most common iron oxide in serpentinites. It is also the main iron oxide produced in experimental and thermodynamic studies of serpentinization (see Sect. 1 for references). Magnetite is emblematic of the high f_{H_2} (and low f_{O_2}) characteristic of serpentinization environments. This is illustrated by our internally controlled (Au capsule) experiments at 300 °C where H_2 accumulates inside the capsule, leading to high-f_{H_2} and thus low-f_{O_2} conditions (Fig. 1a; Table 3). Magnetite forms as the main iron oxide phase (Fig. 5a; Table 2) together with serpentine according to Reaction (R3) (see Sect. 5.2.1). However, magnetite is stable in a wide range of f_{O_2}, being limited by the hematite–magnetite (HM) and iron–magnetite (IM) reactions at high and low f_{O_2} respectively. Note that wüstite (Fe^{2+}_xO) formation is not expected for the relatively low temperatures at which the serpentinization process operates (i.e., < 560–570 °C; Haas and Robie, 1973; Myers and Eugster, 1983). Therefore, the presence of magnetite only provides broad constraints on redox conditions in serpentinites. The occurrence of awaruite (Fe^0_3Ni) in natural (Chamberlain et al., 1965; Frost, 1985; Klein and Bach, 2009) and possibly in experimental (McCollom et al., 2020a, b) serpentinization environments testify to the highly reductive conditions that can be reached ($\Delta IM \approx +1$ according to Frost et al., 2013). Furthermore, awaruite precipitation indicates that H_2-consuming reactions (which reduce part of the Fe^{3+} involved in magnetite formation) are also taking place. This illustrates that the f_{H_2} of serpentinites is determined by the combination of several reactions, some acting in opposed directions.

Our externally (AgPd capsules) controlled experiments carried out at 300 °C demonstrate that hematite ($\alpha Fe^{3+}_2O_3$) appears as a reaction product of a serpentine-producing reaction (Reaction R6; see Sect. 5.2.1). The H_2 generated is continuously extracted and transferred through the permeable capsule to the Ar pressurizing medium (Fig. 1a). Hematite appears in isolation, i.e., without being associated with magnetite as demonstrated by the near baseline MMF in *ol300Pd45* (Fig. 5a). This, as well as the f_{O_2} conditions above the HM buffer in the externally controlled experiments, suggests that hematite is directly formed instead of representing a product from the transformation of an earlier magnetite. Hematite formation has been expected theoretically (e.g., Frost, 1985) and hematite identified as a product phase in thermodynamic modeling of serpentinization reactions (Malvoisin, 2015; Ely et al., 2023). Hematite has also been reported in several experimental studies. It occurs in open-system reactive percolation experiments of CO_2-enriched fluids in olivine aggregates and serpentinite (Peuble et al., 2019; Osselin et al., 2022). Closed-system carbona-

tion of partially serpentinized and weathered peridotites have also yielded hematite-bearing product assemblages (Hövelmann et al., 2011). Lafay et al. (2018) observed the appearance of hematite in closed-system carbonation experiments of olivine single crystals. In contrast, parallel hydration experiments yielded only magnetite without hematite (Lafay et al., 2018). Peuble et al. (2019) assigned the oxidation of Fe^{2+} to the reduction of CO_2 rather than of H_2O as classically proposed in serpentinizing environments. For CO_2-free conditions, hematite appears only in the reactive percolation study of Godard et al. (2013) performed with an oxidizing ingress fluid equilibrated with atmospheric O_2. It is notably absent from the high-pressure closed-system peridotite hydration experiments of Nakatani and Nakamura (2016), despite one buffered at HM. In this particular experiment, the H_2 generated in the reaction chamber was extracted (as in the present study) and consumed to oxidize hematite of the external buffer, and only magnetite formed with serpentine. We conclude that hematite formation in previous studies is a consequence of the addition of an oxidizing chemical component to the system (either CO_2 or O_2). In contrast, in the present study, a causal relation is demonstrated between the presence of hematite and the redox parameters. The appearance of hematite (and the transition from magnetite to hematite) is the result of imposing specific redox conditions (low f_{H_2} and high f_{O_2}) during the serpentinization process.

In natural contexts, iron oxide phases other than magnetite, such as maghemite, have been reported (Prévot et al., 1981; Krammer, 1990; Nazarova et al., 2000). Hematite is also present although rarely found in the serpentinized oceanic crust (Smith and Banerjee, 1985; Bach et al., 2004; Huang et al., 2017a). When present, natural hematite has been interpreted as related to a seawater–rock interaction process that postdates the serpentinization event (Bach et al., 2004). Following the final and most advanced stages of serpentinization, fluid circulations lead to the dissolution of magnetite and its replacement by hematite as the iron oxide phase. This mechanism occurs under oxidizing conditions as indicated by the abundance of hematite in Hole 1268A and iowaite in Hole 1272A (Bach et al., 2004).

5.4 Implication for serpentinization processes at MORs

Experiments of this paper demonstrate that the H_2 mobility has an influence on the serpentinization reaction. The internally controlled f_{H_2} experiments lead to the confinement of H_2, whereas, in the externally controlled f_{H_2} experiments, H_2 is extracted from the reacting serpentinization system. Contrasted redox (reducing vs. oxidizing) conditions and product phase assemblages (magnetite vs. hematite) characterize the two regimes. The experimental methodology implemented for H_2 in this paper is closely analogous to the "internally controlled" vs. "externally controlled" cases classically considered in the modeling of metasomatic processes such as serpentinization (Evans et al., 2013). Below, we use the mobility of H_2 as a proxy of fluid circulation, open vs. closed, in oceanic hydrothermal systems and examine the implications of fluid circulations for redox control of serpentinization processes at MORs.

In our internally controlled f_{H_2} experiments, the f_{H_2} is imposed by the fluid–rock interaction process (serpentinization). This situation is analogous to the one prevailing in rocks having low permeabilities and whose behavior approaches that of a "closed" system. The permeability data available for ultramafic rocks (Villeneuve et al., 2014; Farough et al., 2016; Tutolo et al., 2018) show that such closed-system situations generally apply to non-fractured lithologies. It is also worth emphasizing that, because of the volume expansion that accompanies serpentinization (Kelemen and Hirth, 2012; Evans et al., 2020; Klein and Le Roux, 2020; Malvoisin et al., 2020), porosity will tend to decrease upon hydration of ultramafic rocks, thus lowering their permeability (Tutolo et al., 2018). Ocean floor serpentinites from the MARK area record serpentinization stages formed in a closed, diffusive system, and their high serpentinization rates imply large volume expansions of the rocks (Andreani et al., 2007). Under these conditions, the fluid composition, including the H_2 concentration and the f_{H_2}, will be determined by rock-dominated fluid–rock interactions (e.g., Frost et al., 2013). It is important to emphasize that this is the case of most experimental serpentinization studies, which as a rule are performed with W/R ratios < 3 (Seyfried et al., 2007; Malvoisin et al., 2012a, b; Malvoisin and Brunet, 2014; Klein et al., 2015; McCollom et al., 2016, 2020a, b; Fauguerolles, 2016; Table 2). These studies yield high concentrations of dissolved H_2 (m_{H_2}) in the fluid, high f_{H_2}, and low f_{O_2} (Table 3). Small W/R ratios are also considered some thermodynamic simulations of serpentinization (e.g., McCollom and Bach, 2009; Klein et al., 2013). Natural serpentinites have mineral assemblages that closely correspond to the experimental and thermodynamic simulations. They comprise serpentine, brucite, and magnetite as dominant phases (Mével, 2003; Bach et al., 2006; Klein et al., 2014). Properties of product phases such as magnetite (magnetic properties) are similar between natural and experimental serpentinites (Fig. 5). The common occurrence of awaruite ($FeNi_3$) as an accessory phase (Frost, 1985; Klein and Bach, 2009; Foustoukos et al., 2015) is also consistent with a "closed" system in which conditions are kept reducing because a low permeability.

Although the preceding situation is very close to the one simulated in our serpentinization experiments performed under internal f_{H_2} control, one important difference between natural and experimental systems is to be noted. Experiments all start from oxidized charges and low-f_{H_2} conditions, so the H_2 concentration progressively increases with time and advancement of the reaction. In contrast, in natural systems, rock-buffering through serpentine–brucite–magnetite fluid–mineral equilibria is assumed during the initial stages of serpentinization (Beard et al., 2009; Frost et al., 2013). This im-

plies initially high f_{H_2} and highly reducing conditions, although the influence of initial fluids of variable f_{O_2} has been considered in some simulations (Malvoisin, 2015). This difference in initial f_{O_2} between experimental and natural systems is considered significant. As noted earlier, it is probably responsible for the lack of brucite in our experimental product assemblages.

Our externally controlled f_{H_2} experiments correspond to a situation where the f_{H_2} is imposed from outside the reacting system. This situation is analogous to a serpentinization environment where the f_{H_2} is controlled by an externally derived fluid. We assume that serpentinization is a hydration process driven by seawater and, consequently, the external fluid should have a low f_{H_2}. It is now accepted that serpentinization takes place in an active tectonic environment where fracturing of rock and fluid infiltration are intimately associated (Andreani et al., 2007; Iyer et al., 2008; Plümper et al., 2012; Rouméjon and Cannat, 2014). For example, it has been proposed that mesh texture initiation results from tectonically controlled penetration of seawater-dominated fluids within peridotites and that the last stage of serpentinization takes place in the brittle-fracturing regime where advective fluid transfer dominates (Andreani et al., 2007; Rouméjon and Cannat, 2014). During these two stages, the fluid circulation regime is controlled by active fracturing and thus approaches an "open" system regime. In this case, certain components of the fluid phase can be externally controlled. H_2 almost certainly belongs to this group given its very high mobility, but the other fluid components (e.g., $a_{SiO_{2(aq)}}$) might behave differently. Under this situation, simulated in our externally controlled experiments performed with AgPd capsules, the serpentinization reaction is modified (Reaction (R6); see Sect. 5.2.1). The appearance of hematite as a product of the reaction implies the possibility of low f_{H_2} (high f_{O_2}) during serpentinization and confirms previous expectations (e.g., Frost, 1985). It is worth noting that, in thermodynamic simulations (Malvoisin, 2015; Ely et al., 2023), hematite appears only for elevated W/R ratios (> 20 and > 6.5, respectively), i.e., for conditions analogous to our "open" system situation.

The near-absence of hematite in serpentinized peridotite (Smith and Banerjee, 1985; Bach et al., 2004; Huang et al., 2017a) is probably to be related to the very low f_{H_2} conditions necessary for hematite to be stable in natural hydrothermal oceanic systems ($f_{H_2} < 2.1 \times 10^{-4}$ MPa at 300 °C; Table 1). Such low-f_{H_2} conditions appear to be reached in specific contexts, so a serpentine–hematite–brucite assemblage can be expected to be produced in place of serpentine–magnetite–brucite usually found in serpentinization environments. However, an appropriately low-f_{H_2} range might be rarely attained, and hematite-bearing serpentinites might be difficult to preserve since hematite would presumably react and transform if subjected to later hydrothermal stages involving higher f_{H_2} fluids. Yet, the presence of hematite, although rare, attests to the possibility of low-f_{H_2} conditions either locally or temporarily and, by inference, of varying f_{H_2} during hydration of the oceanic crust. This stresses the need to consider the redox parameters as key process variables in serpentinization environments.

6 Conclusions

Our experiments highlight the key role played by the redox conditions and mechanisms of redox control during serpentinization. We have demonstrated experimentally that serpentinization can take place in a large range of f_{H_2} (and in a correspondingly large range of f_{O_2}). However, although the general mechanism remains the same, notable differences were found between the internally and externally controlled experiments. At 300 °C, in Au capsules (internal f_{H_2} control), H_2 accumulation leads to a relatively high-f_{H_2} (low-f_{O_2}) environment characterized by the serpentine–magnetite assemblage. In comparison, in AgPd capsules (external f_{H_2} control), continuous removal of the produced H_2 yields a low-f_{H_2} (high-f_{O_2}) environment characterized by the serpentine–hematite(–magnetite) assemblage. At 350 °C, the lesser efficiency of the serpentinization reaction limits H_2 production, and both the internally and externally controlled experiments are characterized by the serpentine–hematite(–magnetite) assemblage. The maximum serpentine production is observed at 300 °C under external f_{H_2} control, which is in the optimum temperature range for serpentinization, the reaction being enhanced because of continuous removal of H_2. Differences in product phase assemblages found in this study imply that natural serpentinization reaction mechanisms vary with redox conditions, and consequences for H_2 production fluxes and rates can be expected.

The externally controlled experiments at 300 °C demonstrate that hematite can appear as a product of the serpentinization reaction. In contrast with previous studies where the presence of hematite was the consequence of the addition of an oxidizing chemical component, the present study establishes a causal relation between hematite and the imposed redox variables. The lack of brucite probably reflects conditions insufficiently reducing (f_{H_2} not high enough), and brucite appearance would be expected in longer internally controlled experiments (to promote reaction advancement) and for lower W/R ratios. Brucite would be even more unlikely under low-f_{H_2} environments as in the externally controlled experiments. We emphasize the significant difference between, on the one hand, most serpentinization experiments which start from oxidized, low-f_{H_2} conditions and, on the other hand, natural systems where serpentinization is assumed to start at equilibrium with serpentine–brucite–magnetite and so under high f_{H_2}.

Our experiments under external f_{H_2} control have no counterparts among natural serpentinites mainly because these rocks typically lack hematite. However, the behavior of H_2 and its differential mobility in our two types of experiments has applications for natural oceanic hydrothermal systems.

At MORs, "closed-system" serpentinization stages, marked by low rock permeabilities and small W/R ratios, alternate with serpentinization stages where "open-system" fluid infiltration is driven by tectonic activity and high transient rock permeabilities. The former fluid regime would promote a situation analogous to our experimental internal f_{H_2} control where serpentinization leads to the production of H_2 and its local accumulation. Conversely, in the latter case, the f_{H_2} would be presumably controlled at low values by the infiltrating fluid, similar to our externally controlled experimental simulations. Given the differences noted in product phase assemblages between the two types of experiments, the possibility emerges to correlate the mineralogical composition of serpentinites with fluid circulation regimes in the oceanic crust.

Appendix A: Starting material composition

Compositions of selected starting mineral phases are given in Table A1.

Table A1. Composition of starting minerals.

Component	San Carlos olivine	Åheim olivine	Åheim orthopyroxene
Oxides (wt %)			
SiO_2	40.68	41.26	57.79
TiO_2	0.02	0.02	0.08
Al_2O_3	0.02	0.01	0.10
Cr_2O_3	0.01	0.00	0.00
FeO	9.39	5.80	4.09
MnO	0.13	0.06	0.00
NiO	0.28	0.28	0.00
MgO	49.48	51.98	35.73
CaO	0.05	0.02	0.10
Na_2O	0.01	0.02	0.00
K_2O	0.04	0.00	0.02
Total	100.11	99.45	97.91
Atoms			
O (basis)	4.00	4.00	6.00
Si	1.00	1.00	2.01
Ti	0.00	0.00	0.00
Al	0.00	0.00	0.00
Cr	0.00	0.00	0.00
Fe^{2+}	0.19	0.12	0.12
Mn	0.00	0.00	0.00
Ni	0.01	0.01	0.00
Mg	1.80	1.88	1.85
Ca	0.00	0.00	0.00
Na	0.00	0.00	0.00
K	0.00	0.00	0.00
Atomic ratios (%)			
$\frac{Mg}{Mg+Fe}$	90.45	94.00	93.91

See Sect. 3.4 for measurement conditions.

Appendix B: f_{H_2} of Ar pressurizing medium

The f_{H_2} of the pressurizing gas was determined from independent experiments, all performed at 350 °C, 50 MPa, using pressure vessels, pressurizing gas, capsule materials, and durations identical to the externally f_{H_2}-controlled serpentinization experiments (Table B1). Both indirect and direct measurements are available, the two approaches yielding globally identical results. Indirect constraints on the f_{H_2} come from charges ran with magnetite and hematite (plus water and, in one case, San Carlos olivine). Magnetite systematically oxidized to produce either a hematite-only (Run *A1*) or a hematite-dominant (Run *A2*) product assemblage (Table B1), indicating that the f_{H_2} imposed by the pressurizing gas is lower than that corresponding to the HM buffer ($f_{H_2} = 3.5 \times 10^{-4}$ MPa at 350 °C, 50 MPa; Table 1). Direct constraints were obtained from the hydrogen sensor method of Chou (1987) and Chou and Cygan (1990). AgCl molality of 40 mmol kg^{-1} was measured for the Ar pressurized vessel (Run *A3*), lower than that of the HM reference run (Run *A4*, 72 mmol kg^{-1} on average of *A4a* and *A4b*; Table B1) and yielding a f_{H_2} for the pressurizing gas (0.9×10^{-4} MPa) lower than that corresponding to the HM buffer (3.5×10^{-4} MPa).

Table B1. Experimental constraints on the f_{H_2} of the pressurizing medium.

Run	Capsule material	Starting assemblage	Final assemblage	Comments
A1	$Ag_{25}Pd_{75}$	Mgt–Hm	Hm	Mgt fully oxidized
A2	$Ag_{25}Pd_{75}$	Mgt–Hm–Ol	Mgt–Hm–Ol	Mgt partly oxidized (Hm $\gg$ Mgt)
A3	$Ag_{25}Pd_{75}$	Ag–AgCl	Ag–AgCl	$Cl = 0.040\,mol\,L^{-1}$
A4c	Au	Mgt–Hm	Mgt–Hm	Mgt slightly oxidized
A4a	$Ag_{25}Pd_{75}$	Ag–AgCl	Ag–AgCl	$Cl = 0.118\,mol\,L^{-1}$
A4b	$Ag_{25}Pd_{75}$	Ag–AgCl	Ag–AgCl	$Cl = 0.026\,mol\,L^{-1}$

All experiments performed at 350 °C, 50 MPa, for 31 d, with Ar pressurizing gas and in the same pressure vessels as the serpentinization experiments. For runs *A1*, *A2*, and *A4c*, the starting Mgt/Hm proportion is 80/20 by mass. Run *A4* is the reference run (see Chou, 1987, for details of the hydrogen sensor method). Mineral abbreviations: Mgt: magnetite; Hm: hematite; Ol: San Carlos olivine.

Appendix C: Determination of MMF baseline

The minimum detectable MMF is approximated by the MMF of magnetite-free olivines. The J_s of starting San Carlos olivines of different grain sizes has been measured (Table C1). The corresponding MMF data are fitted with a power law:

$$y = a \times x^b, \tag{C1}$$

where $a = 0.0314$, $b = -0.31$, and x is the grain size. The coefficient of determination (R^2) is 0.971. This expression is used to construct the baselines in Fig. 5.

Table C1. J_s and corresponding MMF of starting magnetite-free olivines as a function of grain size.

Grain size (µm)	J_s ($mA\,m^2\,kg^{-1}$)	MMF (wt %)
500–1000	4.1	0.0044
90–125	6.1	0.0066
45–50	9.0	0.0098
25–32	10.2	0.0111

Code availability. The source code for SUPCRT92 (Johnson et al., 1992) is available on Jim Palandri's (University of Oregon) website: https://pages.uoregon.edu/palandri/.

Data availability. Data in Tables 2, 4, A1, A2, and A3 and in Figs. 2–5 and 7 are original data obtained by the authors for the present study. The other data used in Tables 1 and 3 and in Fig. 6 are from the literature and can be made available upon request.

Author contributions. CF, TC, JV, and MP designed the experiments and CF carried them out. Analytical data acquisition and processing were carried out by CF. CF and MP prepared the manuscript with contributions of TC and JV.

Competing interests. The contact author has declared that none of the authors has any competing interests.

Disclaimer. Publisher's note: Copernicus Publications remains neutral with regard to jurisdictional claims made in the text, published maps, institutional affiliations, or any other geographical representation in this paper. While Copernicus Publications makes every effort to include appropriate place names, the final responsibility lies with the authors.

Special issue statement. This article is part of the special issue "Probing the Earth: magma and fluids, a tribute to the career of Michel Pichavant". It is a result of the Magma & Fluids workshop, Orléans, France, 4–6 July 2022.

Acknowledgements. We thank Claire Carvallo (IMPMC, Paris) and Erwan Le Menn (LPG, Nantes) for their help with magnetic measurements and the Raman analysis, respectively. Ida Di Carlo and Philippe Penhoud helped with the SEM and XRD.

Financial support. This work forms part of Colin Fauguerolles' PhD thesis, which was supported by Région Centre, ANR (project FLUXHYD), and Labex Voltaire.

Review statement. This paper was edited by Olivier Bachmann and reviewed by Carla Tiraboschi and two anonymous referees.

References

Abrajano, T. A., Sturchio, N. C., Kennedy, B. M., Lyon, G. L., Muehlenbachs, K., and Bohlke, J. K.: Geochemistry of reduced gas related to serpentinization of the Zambales ophiolite, Philippines, Appl. Geochem., 5, 625–630, https://doi.org/10.1016/0883-2927(90)90060-I, 1990.

Allen, D. E. and Seyfried Jr., W. E.: Compositional controls on vent fluids from ultramafic-hosted hydrothermal

systems at mid-ocean ridges: An experimental study at 400 °C, 500 bars, Geochim. Cosmochim. Ac., 67, 1531–1542, https://doi.org/10.1016/S0016-7037(02)01173-0, 2003.

Andreani, M., Mével, C., Boullier, A.-M., and Escartin, J.: Dynamic control on serpentine crystallization in veins: constraints on hydration processes in oceanic peridotites, Geochem. Geophy. Geosy., 8, Q02012, https://doi.org/10.1029/2006GC001373, 2007.

Andreani, M., Munoz, M., Marcaillou, C., and Delacour, A.: μXANES study of iron redox state in serpentine during oceanic serpentinization, Lithos, 178, 70–83, https://doi.org/10.1016/j.lithos.2013.04.008, 2013.

Auzende, A.-L., Daniel, I., Reynard, B., Lemaire, C., and Guyot, F.: High-pressure behaviour of serpentine minerals: a Raman spectroscopic study, Phys. Chem. Miner., 31, 269–277, https://doi.org/10.1007/s00269-004-0384-0, 2004.

Bach, W., Garrido, C. J., Paulick, H., Harvey, J., and Rosner, M.: Seawater-peridotite interactions: First insights from ODP Leg 209, MAR 15° N, Geochem. Geophy. Geosy., 5, Q09F26, https://doi.org/10.1029/2004GC000744, 2004.

Bach, W., Paulick, H., Garrido, C. J., Ildefonse, B., Meurer, W. P., and Humphris, S. E.: Unraveling the sequence of serpentinization reactions: petrography, mineral chemistry, and petrophysics of serpentinites from MAR 15° N (ODP Leg 209, Site 1274), Geophys. Res. Lett., 33, L13306, https://doi.org/10.1029/2006GL025681, 2006.

Beard, J. S., Frost, B. R., Fryer, P., McCaig, A., Searle, R., Ildefonse, B., Zinin, P., and Sharma, S. K.: Onset and progression of serpentinization and magnetite formation in olivine-rich troctolite from IODP Hole U1309D, J. Petrol., 50, 387–403, https://doi.org/10.1093/petrology/egp004, 2009.

Berckhemer, H., Kampfmann, W., Aulbach, E., and Schmeling, H.: Shear modulus and Q of forsterite and dunite near partial melting from forced-oscillation experiments, Phys. Earth Planet. In., 29, 30–41, https://doi.org/10.1016/0031-9201(82)90135-2, 1982.

Berndt, M. E., Allen, D. E., and Seyfried Jr., W. E.: Reduction of CO_2 during serpentinization of olivine at 300 °C and 500 bar, Geology, 24, 351–354, https://doi.org/10.1130/0091-7613(1996)024<0351:ROCDSO>2.3.CO;2, 1996.

Burnham, C. W., Holloway, J. R., and Davis, N. F.: Thermodynamic Properties of Water to 1,000 °C and 10,000 bars, Vol. 132, Geological Society of America, https://doi.org/10.1130/SPE132, 1969.

Cannat, M.: Emplacement of mantle rocks in the seafloor at mid-ocean ridges, J. Geophys. Res.-Sol. Ea., 98, 4163–4172, https://doi.org/10.1029/92JB02221, 1993.

Cannat, M., Fontaine, F., and Escartín, J.: Serpentinization and associated hydrogen and methane fluxes at slow spreading ridges, in: Diversity of Hydrothermal Systems on Slow Spreading Ocean Ridges, edited by: Rona, P. A., Devey, C. W., Dyment, J., and Murton, B. J., Vol. 188 of Geophysical Monograph Series, 241–264, American Geophysical Union, Washington, D.C., https://doi.org/10.1029/2008GM000760, 2010.

Chamberlain, J. A., McLeod, C. R., Traill, R. J., and Lachance, G. R.: Native metals in the Muskox intrusion, Can. J. Earth Sci., 2, 188–215, https://doi.org/10.1139/e65-017, 1965.

Charlou, J. L., Donval, J. P., Fouquet, Y., Jean-Baptiste, P., and Holm, N.: Geochemistry of high H_2 and CH_4 vent fluids issuing from ultramafic rocks at the Rainbow hydrothermal field (36°14′ N, MAR), Chem. Geol., 191, 345–359, https://doi.org/10.1016/S0009-2541(02)00134-1, 2002.

Charlou, J. L., Donval, J. P., Konn, C., Ondréas, H., Fouquet, Y., Jean-Baptiste, P., and Fourré, E.: High production and fluxes of H_2 and CH_4 and evidence of abiotic hydrocarbon synthesis by serpentinization in ultramafic-hosted hydrothermal systems on the Mid-Atlantic Ridge, in: Diversity of Hydrothermal Systems on Slow Spreading Ocean Ridges, edited by: Rona, P. A., Devey, C. W., Dyment, J., and Murton, B. J., Vol. 188 of Geophysical Monograph Series, 265–296, American Geophysical Union, Washington, D.C., https://doi.org/10.1029/2008GM000752, 2010.

Chou, I.-M.: Permeability of precious metals to hydrogen at 2 kb total pressure and elevated temperatures, Am. J. Sci., 286, 638–658, https://doi.org/10.2475/ajs.286.8.638, 1986.

Chou, I.-M.: Oxygen buffer and hydrogen sensor techniques at elevated pressures and temperatures, in: Hydrothermal Experimental Techniques, edited by: Ulmer, G. C. and Barnes, H. L., 61–99, John Wiley and Sons, New York, NY, 1987.

Chou, I.-M. and Cygan, G. L.: Quantitative redox control and measurement in hydrothermal experiments, in: Fluid-mineral Interactions: A Tribute to H. P. Eugster, edited by: Spencer, R. J. and Chou, I. M., Vol. 2 of Geochemical Society: Special publication, 3–15, Geochemical Society, ISBN 0-941809-01-3, 1990.

Cullity, B. D.: Introduction to Magnetic Materials, Addison-Wiley Publishing Company, New Jersey, ISBN 0201012189, 1972.

Day, R., Fuller, M., and Schmidt, V. A.: Hysteresis properties of titanomagnetites: grain-size and compositional dependence, Phys. Earth Planet. In., 13, 260–267, https://doi.org/10.1016/0031-9201(77)90108-X, 1977.

de Faria, D. L. A., Venâncio Silva, S., and de Oliveira, M. T.: Raman microspectroscopy of some iron oxides and oxyhydroxides, J. Raman Spectrosc., 28, 873–878, https://doi.org/10.1002/(SICI)1097-4555(199711)28:11<873::AID-JRS177>3.0.CO;2-B, 1997.

Drummond Jr., S. E.: Boiling and Mixing of Hydrothermal Fluids: Chemical Effects on Mineral Precipitation, PhD thesis, The Pennsylvania State University, 1981.

Dunlop, D. J.: Theory and application of the Day plot (M_{rs}/M_s versus H_{cr}/H_c) 1. Theoretical curves and tests using titanomagnetite data, J. Geophys. Res.-Sol. Ea., 107, EPM 4-1–EPM 4-22, https://doi.org/10.1029/2001JB000486, 2002.

Ely, T. D., Leong, J. M., Canovas, P. A., and Shock, E. L.: Huge variation in H_2 generation during seawater alteration of ultramafic rocks, Geochem. Geophy. Geosy., 24, e2022GC010658, https://doi.org/10.1029/2022GC010658, 2023.

Escartín, J., Hirth, G., and Evans, B.: Effects of serpentinization on the lithospheric strength and the style of normal faulting at slow-spreading ridges, Earth Planet. Sc. Lett., 151, 181–189, https://doi.org/10.1016/S0012-821X(97)81847-X, 1997.

Escartín, J., Hirth, G., and Evans, B.: Strength of slightly serpentinized peridotites: Implications for the tectonics of oceanic lithosphere, Geology, 29, 1023–1026, https://doi.org/10.1130/0091-7613(2001)029<1023:SOSSPI>2.0.CO;2, 2001.

Eugster, H. P.: Heterogeneous reactions involving oxidation and reduction at high pressures and temperatures, J. Chem. Phys., 26, 1760–1761, https://doi.org/10.1063/1.1743626, 1957.

Eugster, H. P. and Skippen, G. B.: Igneous and metamorphic reactions involving gas equilibria, in: Researches in geochemistry,

edited by: Abelson, P. H., Vol. 2, 492–520, John Wiley and Sons, New York, NY, 1967.

Evans, B. W.: Control of the products of serpentinization by the $Fe^{2+}Mg_{-1}$ exchange potential of olivine and orthopyroxene, J. Petrol., 49, 1873–1887, https://doi.org/10.1093/petrology/egn050, 2008.

Evans, K. A., Powell, R., and Frost, B. R.: Using equilibrium thermodynamics in the study of metasomatic alteration, illustrated by an application to serpentinites, Lithos, 168, 67–84, https://doi.org/10.1016/j.lithos.2013.01.016, 2013.

Evans, O., Spiegelman, M., and Kelemen, P. B.: Phase-field modeling of reaction-driven cracking: Determining conditions for extensive olivine serpentinization, J. Geophys. Res.-Sol. Ea., 125, e2019JB018614, https://doi.org/10.1029/2019JB018614, 2020.

Farough, A., Moore, D. E., Lockner, D. A., and Lowell, R. P.: Evolution of fracture permeability of ultramafic rocks undergoing serpentinization at hydrothermal conditions: An experimental study, Geochem. Geophy. Geosy., 17, 44–55, https://doi.org/10.1002/2015GC005973, 2016.

Fauguerolles, C.: Étude expérimentale de la production d'H_2 associée à la serpentinisation des péridotites au niveau des dorsales océaniques lentes, Quantification – États rédox – Mécanismes réactionnels, PhD thesis, Université d'Orléans, https://theses.hal.science/tel-01549129 (last access: 27 June 2024), 2016.

Fonteilles, M.: Les mécanismes de la métasomatose, B. Minéral., 101, 166–194, https://doi.org/10.3406/bulmi.1978.7185, 1978.

Foustoukos, D. I., Bizimis, M., Frisby, C., and Shirey, S. B.: Redox controls on Ni-Fe-PGE mineralization and Re/Os fractionation during serpentinization of abyssal peridotite, Geochim. Cosmochim. Ac., 150, 11–25, https://doi.org/10.1016/j.gca.2014.11.025, 2015.

Frost, B. R.: On the stability of sulfides, oxides, and native metals in serpentinite, J. Petrol., 26, 31–63, https://doi.org/10.1093/petrology/26.1.31, 1985.

Frost, B. R. and Beard, J. S.: On silica activity and serpentinization, J. Petrol., 48, 1351–1368, https://doi.org/10.1093/petrology/egm021, 2007.

Frost, B. R., Evans, K. A., Swapp, S. M., Beard, J. S., and Mothersole, F. E.: The process of serpentinization in dunite from New Caledonia, Lithos, 178, 24–39, https://doi.org/10.1016/j.lithos.2013.02.002, 2013.

Garrels, R. M. and Thompson, M. E.: A chemical model for sea water at 25 °C and one atmosphere total pressure, Am. J. Sci., 260, 57–66, https://doi.org/10.2475/ajs.260.1.57, 1962.

Godard, M., Luquot, L., Andreani, M., and Gouze, P.: Incipient hydration of mantle lithosphere at ridges: A reactive-percolation experiment, Earth Planet. Sc. Lett., 371, 92–102, https://doi.org/10.1016/j.epsl.2013.03.052, 2013.

Gunter, W. D., Myers, J., and Girsperger, S.: Hydrogen: Metal Membranes, in: Hydrothermal Experimental Techniques, edited by: Ulmer, G. C. and Barnes, H. L., 100–120, John Wiley and Sons, New York, NY, 1987.

Haas, J. L. and Robie, R. A.: Thermodynamic data for wustite, $Fe_{0.947}O$, magnetite, Fe_3O_4, and hematite, Fe_2O_3, in: Transactions-American Geophysical Union, Vol. 54, p. 483, American Geophysical Union, Whashinton DC, https://doi.org/10.1029/EO054i005p00222, 1973.

Harvie, C., Weare, J. H., and O'Keefe, M.: Permeation of hydrogen through platinum: A re-evaluation of the data of Chou *et al*, Geochim. Cosmochim. Ac., 44, 899–900, https://doi.org/10.1016/0016-7037(80)90271-9, 1980.

Hövelmann, J., Austrheim, H., Beinlich, A., and Munz, I. A.: Experimental study of the carbonation of partially serpentinized and weathered peridotites, Geochim. Cosmochim. Ac., 75, 6760–6779, https://doi.org/10.1016/j.gca.2011.08.032, 2011.

Huang, R., Lin, C.-T., Sun, W., Ding, X., Zhan, W., and Zhu, J.: The production of iron oxide during peridotite serpentinization: Influence of pyroxene, Geosci. Front., 8, 1311–1321, https://doi.org/10.1016/j.gsf.2017.01.001, 2017a.

Huang, R., Song, M., Ding, X., Zhu, S., Zhan, W., and Sun, W.: Influence of pyroxene and spinel on the kinetics of peridotite serpentinization, J. Geophys. Res.-Sol. Ea., 122, 7111–7126, https://doi.org/10.1002/2017JB014231, 2017b.

Huang, R., Sun, W., Song, M., and Ding, X.: Influence of pH on molecular hydrogen (H_2) generation and reaction rates during serpentinization of peridotite and olivine, Minerals, 9, 661, https://doi.org/10.3390/min9110661, 2019.

Iyer, K., Jamtveit, B., Mathiesen, J., Malthe-Sørenssen, A., and Feder, J.: Reaction-assisted hierarchical fracturing during serpentinization, Earth Planet. Sc. Lett., 267, 503–516, https://doi.org/10.1016/j.epsl.2007.11.060, 2008.

Jackson, I., Paterson, M. S., and Gerald, J. D. F.: Seismic wave dispersion and attenuation in Åheim dunite: an experimental study, Geophys. J. Int., 108, 517–534, https://doi.org/10.1111/j.1365-246X.1992.tb04633.x, 1992.

Janecky, D. R. and Seyfried, W. E.: Hydrothermal serpentinization of peridotite within the oceanic crust: experimental investigations of mineralogy and major element chemistry, Geochim. Cosmochim. Ac., 50, 1357–1378, https://doi.org/10.1016/0016-7037(86)90311-X, 1986.

Johnson, J. W., Oelkers, E. H., and Helgeson, H. C.: SUPCRT92: A software package for calculating the standard molal thermodynamic properties of minerals, gases, aqueous species, and reactions from 1–5000 bar and 0–1000 °C, Comput. Geosci., 18, 899–947, https://doi.org/10.1016/0098-3004(92)90029-Q, 1992 (code available at: https://pages.uoregon.edu/palandri/, last access: 20 June 2024).

Karson, J. A., Thompson, G., Humphris, S. E., Edmond, J. M., Bryan, W. B., Brown, J. R., Winters, A. T., Pockalny, R. A., Casey, J. F., Campbell, A. C., Klinkhammer, G., Palmer, M. R., Kinzler, R. J., and Sulanowska, M. M.: Along-axis variations in seafloor spreading in the MARK area, Nature, 328, 681–685, https://doi.org/10.1038/328681a0, 1987.

Kelemen, P. B. and Hirth, G.: Reaction-driven cracking during retrograde metamorphism: Olivine hydration and carbonation, Earth Planet. Sc. Lett., 345, 81–89, https://doi.org/10.1016/j.epsl.2012.06.018, 2012.

Kelemen, P. B. and Matter, J.: *In situ* carbonation of peridotite for CO_2 storage, P. Natl. Acad. Sci. USA, 105, 17295–17300, https://doi.org/10.1073/pnas.0805794105, 2008.

Khisina, N. R., Khramov, D. A., Kleschev, A. A., and Langer, K.: Laihunitization as a mechanism of olivine oxidation, Eur. J. Mineral., 10, 229–238, https://doi.org/10.1127/ejm/10/2/0229, 1998.

Klein, F. and Bach, W.: Fe-Ni-Co-O-S phase relations in peridotite-seawater interactions, J. Petrol., 50, 37–59, https://doi.org/10.1093/petrology/egn071, 2009.

Klein, F. and Le Roux, V.: Quantifying the volume increase and chemical exchange during serpentinization, Geology, 48, 552–556, https://doi.org/10.1130/G47289.1, 2020.

Klein, F. and McCollom, T. M.: From serpentinization to carbonation: new insights from a CO_2 injection experiment, Earth Planet. Sc. Lett., 379, 137–145, https://doi.org/10.1016/j.epsl.2013.08.017, 2013.

Klein, F., Bach, W., Jöns, N., McCollom, T., Moskowitz, B., and Berquó, T.: Iron partitioning and hydrogen generation during serpentinization of abyssal peridotites from 15° N on the Mid-Atlantic Ridge, Geochim. Cosmochim. Ac., 73, 6868–6893, https://doi.org/10.1016/j.gca.2009.08.021, 2009.

Klein, F., Bach, W., and McCollom, T. M.: Compositional controls on hydrogen generation during serpentinization of ultramafic rocks, Lithos, 178, 55–69, https://doi.org/10.1016/j.lithos.2013.03.008, 2013.

Klein, F., Bach, W., Humphris, S. E., Kahl, W.-A., Jöns, N., Moskowitz, B., and Berquó, T. S.: Magnetite in seafloor serpentinite – Some like it hot, Geology, 42, 135–138, https://doi.org/10.1130/G35068.1, 2014.

Klein, F., Grozeva, N. G., Seewald, J. S., McCollom, T. M., Humphris, S. E., Moskowitz, B., Berquó, T. S., and Kahl, W.-A.: Fluids in the crust. Experimental constraints on fluid-rock reactions during incipient serpentinization of harzburgite, Am. Mineral., 100, 991–1002, https://doi.org/10.2138/am-2015-5112, 2015.

Klein, F., Grozeva, N. G., and Seewald, J. S.: Abiotic methane synthesis and serpentinization in olivine-hosted fluid inclusions, P. Natl. Acad. Sci. USA, 116, 17666–17672, https://doi.org/10.1073/pnas.1907871116, 2019.

Knafelc, J., Filiberto, J., Ferré, E. C., Conder, J. A., Costello, L., Crandall, J. R., Dyar, M. D., Friedman, S. A., Hummer, D. R., and Schwenzer, S. P.: The effect of oxidation on the mineralogy and magnetic properties of olivine, Am. Mineral., 104, 694–702, https://doi.org/10.2138/am-2019-6829, 2019.

Korzhinskii, D. S.: The theory of systems with perfectly mobile components and processes of mineral formation, Am. J. Sci., 263, 193–205, https://doi.org/10.2475/ajs.263.3.193, 1965.

Krammer, K.: Rock magnetic properties and opaque mineralogy of selected samples from Hole 670A, in: Proceedings of the Ocean Drilling Program, Scientific Results, edited by: Detrick, R., Honnorez, J., Bryan, W. B., Juteau, T., and et al., Vol. 106/109, College Station, TX (Ocean Drilling Program), 269–273, https://doi.org/10.2973/odp.proc.sr.106109.154.1990, 1990.

Lafay, R., Montes-Hernandez, G., Janots, E., Chiriac, R., Findling, N., and Toche, F.: Mineral replacement rate of olivine by chrysotile and brucite under high alkaline conditions, J. Crystal Growth, 347, 62–72, https://doi.org/10.1016/j.jcrysgro.2012.02.040, 2012.

Lafay, R., Montes-Hernandez, G., Renard, F., and Vonlanthen, P.: Intracrystalline reaction-induced cracking in olivine evidenced by hydration and carbonation experiments, Minerals, 8, 412, https://doi.org/10.3390/min8090412, 2018.

Lamadrid, H. M., Rimstidt, J. D., Schwarzenbach, E. M., Klein, F., Ulrich, S., Dolocan, A., and Bodnar, R. J.: Effect of water activity on rates of serpentinization of olivine, Nat. Commun., 8, 16107, https://doi.org/10.1038/ncomms16107, 2017.

Lamadrid, H. M., Zajacz, Z., Klein, F., and Bodnar, R. J.: Synthetic fluid inclusions XXIII. Effect of temperature and fluid composition on rates of serpentinization of olivine, Geochim. Cosmochim. Ac., 292, 285–308, https://doi.org/10.1016/j.gca.2020.08.009, 2021.

Lazar, C.: Using silica activity to model redox-dependent fluid compositions in serpentinites from 100 to 700 °C and from 1 to 20 kbar, J. Petrol., 61, egaa101, https://doi.org/10.1093/petrology/egaa101, 2020.

Legodi, M. A. and de Waal, D.: The preparation of magnetite, goethite, hematite and maghemite of pigment quality from mill scale iron waste, Dyes Pigments, 74, 161–168, https://doi.org/10.1016/j.dyepig.2006.01.038, 2007.

Lemaire, C.: Application des Spectroscopies Vibrationnelles à la Détection d'Amiante dans les Matériaux et à l'Étude des Serpentines, PhD thesis, Paris 7, 2000.

Maffione, M., Morris, A., Plümper, O., and van Hinsbergen, D. J. J.: Magnetic properties of variably serpentinized peridotites and their implication for the evolution of oceanic core complexes, Geochem. Geophy. Geosy., 15, 923–944, https://doi.org/10.1002/2013GC004993, 2014.

Malvoisin, B.: Mass transfer in the oceanic lithosphere: Serpentinization is not isochemical, Earth Planet. Sc. Lett., 430, 75–85, https://doi.org/10.1016/j.epsl.2015.07.043, 2015.

Malvoisin, B. and Brunet, F.: Water diffusion-transport in a synthetic dunite: Consequences for oceanic peridotite serpentinization, Earth Planet. Sc. Lett., 403, 263–272, https://doi.org/10.1016/j.epsl.2014.07.004, 2014.

Malvoisin, B., Brunet, F., Carlut, J., Rouméjon, S., and Cannat, M.: Serpentinization of oceanic peridotites: 2. Kinetics and processes of San Carlos olivine hydrothermal alteration, J. Geophys. Res.-Sol. Ea., 117, B04102, https://doi.org/10.1029/2011JB008842, 2012a.

Malvoisin, B., Carlut, J., and Brunet, F.: Serpentinization of oceanic peridotites: 1. A high-sensitivity method to monitor magnetite production in hydrothermal experiments, J. Geophys. Res.-Sol. Ea., 117, B01104, https://doi.org/10.1029/2011JB008612, 2012b.

Malvoisin, B., Zhang, C., Müntener, O., Baumgartner, L. P., Kelemen, P. B., and ODP Science Party: Measurement of volume change and mass transfer during serpentinization: Insights from the Oman Drilling Project, J. Geophys. Res.-Sol. Ea., 125, e2019JB018877, https://doi.org/10.1029/2019JB018877, 2020.

Marcaillou, C., Munoz, M., Vidal, O., Parra, T., and Harfouche, M.: Mineralogical evidence for H_2 degassing during serpentinization at 300 °C/300 bar, Earth Planet. Sc. Lett., 303, 281–290, https://doi.org/10.1016/j.epsl.2011.01.006, 2011.

Martin, B. and Fyfe, W. S.: Some experimental and theoretical observations on the kinetics of hydration reactions with particular reference to serpentinization, Chem. Geol., 6, 185–202, https://doi.org/10.1016/0009-2541(70)90018-5, 1970.

Mayhew, L. E., Ellison, E. T., McCollom, T. M., Trainor, T. P., and Templeton, A. S.: Hydrogen generation from low-temperature water-rock reactions, Nat. Geosci., 6, 478–484, https://doi.org/10.1038/ngeo1825, 2013.

McCollom, T. M. and Bach, W.: Thermodynamic constraints on hydrogen generation during serpentinization of ultramafic rocks, Geochim. Cosmochim. Ac., 73, 856–875, https://doi.org/10.1016/j.gca.2008.10.032, 2009.

McCollom, T. M. and Seewald, J. S.: A reassessment of the potential for reduction of dissolved CO_2 to hydrocarbons during serpen-

tinization of olivine, Geochim. Cosmochim. Ac., 65, 3769–3778, https://doi.org/10.1016/S0016-7037(01)00655-X, 2001.

McCollom, T. M., Klein, F., Robbins, M., Moskowitz, B., Berquó, T. S., Jöns, N., Bach, W., and Templeton, A.: Temperature trends for reaction rates, hydrogen generation, and partitioning of iron during experimental serpentinization of olivine, Geochim. Cosmochim. Ac., 181, 175–200, https://doi.org/10.1016/j.gca.2016.03.002, 2016.

McCollom, T. M., Klein, F., Moskowitz, B., Berquó, T. S., Bach, W., and Templeton, A. S.: Hydrogen generation and iron partitioning during experimental serpentinization of an olivine-pyroxene mixture, Geochim. Cosmochim. Ac., 282, 55–75, https://doi.org/10.1016/j.gca.2020.05.016, 2020a.

McCollom, T. M., Klein, F., Solheid, P., and Moskowitz, B.: The effect of pH on rates of reaction and hydrogen generation during serpentinization, Philos. T. R. Soc. A, 378, 20180428, https://doi.org/10.1098/rsta.2018.0428, 2020b.

Mével, C.: Serpentinization of abyssal peridotites at mid-ocean ridges, C.R. Geosci., 335, 825–852, https://doi.org/10.1016/j.crte.2003.08.006, 2003.

Moody, J. B.: An experimental study on the serpentinization of iron-bearing olivines, Can. Mineral., 14, 462–478, 1976.

Myers, J. and Eugster, H. P.: The system Fe-Si-O: Oxygen buffer calibrations to 1,500 K, Contrib. Mineral. Petr., 82, 75–90, https://doi.org/10.1007/BF00371177, 1983.

Nakatani, T. and Nakamura, M.: Experimental constraints on the serpentinization rate of fore-arc peridotites: Implications for the upwelling condition of the slab-derived fluid, Geochem. Geophy. Geosy., 17, 3393–3419, https://doi.org/10.1002/2016GC006295, 2016.

Nazarova, K. A., Wasilewski, P. J., and Dick, H. J. B.: Magnetic study of serpentinized harzburgites from the Islas Orcadas Fracture Zone, Mar. Geophys. Res., 21, 475–488, https://doi.org/10.1023/A:1026550011802, 2000.

Neal, C. and Stanger, G.: Hydrogen generation from mantle source rocks in Oman, Earth Planet. Sc. Lett., 66, 315–320, https://doi.org/10.1016/0012-821X(83)90144-9, 1983.

Oelkers, E. H., Declercq, J., Saldi, G. D., Gislason, S. R., and Schott, J.: Olivine dissolution rates: A critical review, Chem. Geol., 500, 1–19, https://doi.org/10.1016/j.chemgeo.2018.10.008, 2018.

Ogasawara, Y., Okamoto, A., Hirano, N., and Tsuchiya, N.: Coupled reactions and silica diffusion during serpentinization, Geochim. Cosmochim. Ac., 119, 212–230, https://doi.org/10.1016/j.gca.2013.06.001, 2013.

Okamoto, A., Ogasawara, Y., Ogawa, Y., and Tsuchiya, N.: Progress of hydration reactions in olivine-H_2O and orthopyroxenite-H_2O systems at 250 °C and vapor-saturated pressure, Chem. Geol., 289, 245–255, https://doi.org/10.1016/j.chemgeo.2011.08.007, 2011.

Osselin, F., Pichavant, M., Champallier, R., Ulrich, M., and Raimbourg, H.: Reactive transport experiments of coupled carbonation and serpentinization in a natural serpentinite. Implication for hydrogen production and carbon geological storage, Geochim. Cosmochim. Ac., 318, 165–189, https://doi.org/10.1016/j.gca.2021.11.039, 2022.

Oufi, O., Cannat, M., and Horen, H.: Magnetic properties of variably serpentinized abyssal peridotites, J. Geophys. Res.-Sol. Ea., 107, EPM 3-1–EPM 3-19, https://doi.org/10.1029/2001JB000549, 2002.

Oyanagi, R., Okamoto, A., and Tsuchiya, N.: Silica controls on hydration kinetics during serpentinization of olivine: Insights from hydrothermal experiments and a reactive transport model, Geochim. Cosmochim. Ac., 270, 21–42, https://doi.org/10.1016/j.gca.2019.11.017, 2020.

Peuble, S., Godard, M., Gouze, P., Leprovost, R., Martinez, I., and Shilobreeva, S.: Control of CO_2 on flow and reaction paths in olivine-dominated basements: An experimental study, Geochim. Cosmochim. Ac., 252, 16–38, https://doi.org/10.1016/j.gca.2019.02.007, 2019.

Pichavant, M.: Effects of B and H_2O on liquidus phase relations in the haplogranite system at 1 kbar, Am. Mineral., 72, 1056–1070, 1987.

Plümper, O., Røyne, A., Magrasó, A., and Jamtveit, B.: The interface-scale mechanism of reaction-induced fracturing during serpentinization, Geology, 40, 1103–1106, https://doi.org/10.1130/G33390.1, 2012.

Prévot, M., Lecaille, A., and Mankinen, E. A.: Magnetic effects of maghemitization of oceanic crust, J. Geophys. Res.-Sol. Ea., 86, 4009–4020, https://doi.org/10.1029/JB086iB05p04009, 1981.

Rouméjon, S. and Cannat, M.: Serpentinization of mantle-derived peridotites at mid-ocean ridges: Mesh texture development in the context of tectonic exhumation, Geochem. Geophy. Geosy., 15, 2354–2379, https://doi.org/10.1002/2013GC005148, 2014.

Rouméjon, S., Cannat, M., Agrinier, P., Godard, M., and Andreani, M.: Serpentinization and fluid pathways in tectonically exhumed peridotites from the Southwest Indian Ridge (62–65° E), J. Petrol., 56, 703–734, https://doi.org/10.1093/petrology/egv014, 2015.

rruff.info: Magnetite R061111, https://rruff.info/)/R061111, last access: 11 August 2023.

Rudert, V., Chou, I.-M., and Eugster, H. P.: Temperature gradients in rapid-quench cold-seal pressure vessels, Am. Mineral., 61, 1012–1015, 1976.

Scaillet, B., Pichavant, M., Roux, J., Humbert, G., and Lefevre, A.: Improvements of the Shaw membrane technique for measurement and control of f_{H_2} at high temperatures and pressures, Am. Mineral., 77, 647–655, 1992.

Schmidt, B. C., Scaillet, B., and Holtz, F.: Accurate control of f_{H_2} in cold-seal pressure vessels with the Shaw membrane technique, Eur. J. Mineral., 7, 893–904, https://doi.org/10.1127/ejm/7/4/0893, 1995.

Schwartz, S., Guillot, S., Reynard, B., Lafay, R., Debret, B., Nicollet, C., Lanari, P., and Auzende, A. L.: Pressure–temperature estimates of the lizardite/antigorite transition in high pressure serpentinites, Lithos, 178, 197–210, https://doi.org/10.1016/j.lithos.2012.11.023, 2013.

Seyfried Jr., W. E. and Dibble Jr., W. E.: Seawater-peridotite interaction at 300 °C and 500 bars: implications for the origin of oceanic serpentinites, Geochim. Cosmochim. Ac., 44, 309–321, https://doi.org/10.1016/0016-7037(80)90139-8, 1980.

Seyfried Jr., W. E., Foustoukos, D. I., and Fu, Q.: Redox evolution and mass transfer during serpentinization: An experimental and theoretical study at 200 °C, 500 bar with implications for ultramafic-hosted hydrothermal systems at Mid-Ocean Ridges, Geochim. Cosmochim. Ac., 71, 3872–3886, https://doi.org/10.1016/j.gca.2007.05.015, 2007.

Seyfried Jr., W. E., Pester, N. J., Ding, K., and Rough, M.: Vent fluid chemistry of the Rainbow hydrothermal system (36° N, MAR): Phase equilibria and in situ pH controls on subseafloor alteration processes, Geochim. Cosmochim. Ac., 75, 1574–1593, https://doi.org/10.1016/j.gca.2011.01.001, 2011.

Seyfried Jr., W. E., Pester, N. J., Tutolo, B. M., and Ding, K.: The Lost City hydrothermal system: Constraints imposed by vent fluid chemistry and reaction path models on subseafloor heat and mass transfer processes, Geochim. Cosmochim. Ac., 163, 59–79, https://doi.org/10.1016/j.gca.2015.04.040, 2015.

Shaw, H. R.: Hydrogen-water vapor mixtures: control of hydrothermal atmospheres by hydrogen osmosis, Science, 139, 1220–1222, https://doi.org/10.1126/science.139.3560.1220, 1963.

Shaw, H. R. and Wones, D. R.: Fugacity coefficients for hydrogen gas between 0 degrees and 1000 degrees C, for pressures to 3000 atm, Am. J. Sci., 262, 918–929, https://doi.org/10.2475/ajs.262.7.918, 1964.

Sleep, N. H., Meibom, A., Fridriksson, T., Coleman, R. G., and Bird, D. K.: H_2 – rich fluids from serpentinization: geochemical and biotic implications, P. Natl. Acad. Sci. USA, 101, 12818–12823, https://doi.org/10.1073/pnas.0405289101, 2004.

Smith, G. M. and Banerjee, S. K.: Magnetic-properties of plutonic rocks from the central North-Atlantic Ocean, in: Initial Reports of the Deep Sea Drilling Project, edited by: Bougault, H., Cande, S. C., Brannon, J. C., Christie, D. M., Clark, M., Curtis, D. M., Drake, N., Echols, D., Ashley Hill, I., Javed Khan, M., Mills, W., Neuser, R., Rideout, M. L., and Weaver, B. L., Vol. 82, 377–383, U.S. Government Printing Office, Washington, D.C., USA, https://doi.org/10.2973/dsdp.proc.82.117.1985, 1985.

Steefel, C. I., DePaolo, D. J., and Lichtner, P. C.: Reactive transport modeling: An essential tool and a new research approach for the Earth sciences, Earth Planet. Sc. Lett., 240, 539–558, https://doi.org/10.1016/j.epsl.2005.09.017, 2005.

Syverson, D. D., Tutolo, B. M., Borrok, D. M., and Seyfried Jr., W. E.: Serpentinization of olivine at 300 °C and 500 bars: an experimental study examining the role of silica on the reaction path and oxidation state of iron, Chem. Geol., 475, 122–134, https://doi.org/10.1016/j.chemgeo.2017.11.006, 2017.

Toft, P. B., Arkani-Hamed, J., and Haggerty, S. E.: The effects of serpentinization on density and magnetic susceptibility: a petrophysical model, Phys. Earth Planet. In., 65, 137–157, https://doi.org/10.1016/0031-9201(90)90082-9, 1990.

Tutolo, B. M., Luhmann, A. J., Tosca, N. J., and Seyfried Jr., W. E.: Serpentinization as a reactive transport process: the brucite silicification reaction, Earth Planet. Sc. Lett., 484, 385–395, https://doi.org/10.1016/j.epsl.2017.12.029, 2018.

Villeneuve, J., Fauguerolles, C., Castelain, T., and Pichavant, M.: Étude expérimentale de l'évolution de la perméabilité des péridotites lors de la serpentinisation, 24ème Réunion des Sciences de la Terre, Pau, France, https://rst2014-pau.sciencesconf.org/conference/rst2014-pau/rstabstractsnum.pdf (last access: 27 June 2024), 2014.

Wegner, W. W. and Ernst, W. G.: Experimentally determined hydration and dehydration reaction rates in the system MgO-SiO_2-H_2O, in: Studies in Metamorphism and Metasomatism, edited by: Greenwood, H. J., Vol. 283-A, 151–180, American Journal of Science, New Haven, Connecticut, 1983.

Weill, D. F. and Fyfe, W. S.: A discussion of the Korzhinskii and Thompson treatment of thermodynamic equilibrium in open systems, Geochim. Cosmochim. Ac., 28, 565–576, https://doi.org/10.1016/0016-7037(64)90077-8, 1964.